Regulation of cellular structure and function through amphipathic motifs

Lin Zhang

A dissertation

submitted in partial fulfillment of the

requirements for the degree of

Master of Science

University of Washington

Year 2025

Committee:

Jihong Bai

Bill Mahoney

Jia Zhu

Program Authorized to Offer Degree:

Laboratory Medicine and Pathology

University of Washington

Abstract

Regulation of cellular structure and function through amphipathic motifs

Lin Zhang

Chair of the Supervisory Committee:
Jihong Bai
Biochemistry

Curvature-sensing mechanisms assist proteins in executing particular actions on various membrane organelles. Here, we investigate the functional specificity of curvature-sensing amphipathic motifs in *Caenorhabditis elegans* through the study of endophilin, an endocytic protein for synaptic vesicle recycling. We generate chimeric endophilin proteins by replacing the endophilin amphipathic motif H0 with other curvature-sensing amphipathic motifs. We find that the role of amphipathic motifs cannot simply be extrapolated from the identity of their parental proteins. For example, the amphipathic motif of the nuclear pore complex protein NUP133 functionally replaces the synaptic role of endophilin H0. Interestingly, non-functional endophilin chimeras have similar defects—producing fewer synaptic vesicles but more endosomes—and this

indicates that the curvature-sensing motifs in these chimeras have a common deficiency for reforming synaptic vesicles. Finally, we convert non-functional endophilin chimeras into functional proteins by changing the cationic property of amphipathic motifs, successfully reprogramming the functional specificity of curvature-sensing motifs *in vivo*.

TABLE OF CONTENTS

LIST OF FIGURES ii
Chapter 2 Figures ii
Chapter 3 Figures ii
Chapter 1. Introduction 1
1.1 The Complexity of Membrane Organization in Eukaryotic Cells 1
1.2 Curvature-Sensing Mechanisms 2
1.3 Biophysical and Biochemical Principles Governing Curvature Sensitivity 3
1.4 Functional Specificity of Curvature-Sensing Motifs of Endophilin A1 4
Chapter 2. The endophilin curvature-sensitive motif requires electrostatic guidance to recycle synaptic vesicles *in vivo* 7
2.1 Summary 8
2.2 Introduction 8
2.3 Results 11
2.4 Discussion 19
2.5 Acknowledgments 23
2.6 Figure Legends 24
2.7 STAR Methods 44
2.8 METHOD DETAILS 47
Chapter 3. Research Progress Report 55
3.1 Overview 55
3.2 Significance and Research Progress 56
3.3 Future Directions 58
Bibliography 60

LIST OF FIGURES

Chapter 2 Figures

Figure 1. 1 32
Figure 1. 2 33
Figure 1. 3 34
Figure 1. 4 35
Figure 1. 5 36
Figure 1. 6 37
Figure 1. 7 38

Suppl. figure 1 39
Suppl. figure 2 40
Suppl. figure 3 41
Suppl. figure 4 42
Suppl. figure 5 43
Suppl. figure 6 43

Chapter 3 Figures

Figure 2. 1 55
Figure 2. 2 57

Chapter 1. Introduction

1.1 The Complexity of Membrane Organization in Eukaryotic Cells

Biological membranes play a central role in shaping the internal organization and functional identity of eukaryotic cells. Rather than acting as inert boundaries, membranes serve as dynamic platforms that facilitate signal transduction, molecular transport, metabolism, and cytoskeletal organization. The compartmentalization of the cytoplasm into organelles depends on the distinct molecular composition and morphology of each membrane-bound structure. Among these defining features, membrane curvature is increasingly recognized as a critical determinant of organelle function (McMahon and Boucrot, 2015; Kozlov et al., 2014).

Organelles exhibit a wide spectrum of curvature profiles. The endoplasmic reticulum contains flat sheets interspersed with tubular extensions, while the Golgi apparatus consists of stacked cisternae. Mitochondria have highly curved inner membranes forming cristae, and vesicular compartments such as endosomes and transport vesicles are typically spherical. Even the plasma membrane displays curvature-rich features like pits, protrusions, and vesicles. These shape differences are not incidental, rather they directly impact trafficking, fusion and fission processes, and protein sorting (Shibata et al., 2009; van Meer et al., 2008).

The generation and recognition of membrane curvature depend on a combination of lipid properties, mechanical forces, and protein interactions. Curved membranes are associated with packing defects, surface tension, and asymmetric lipid distributions that can influence how proteins engage with the bilayer (Antonny, 2011; Zimmerberg and Kozlov, 2006). Proteins that detect or stabilize curved membranes often carry structural modules that convert physical curvature into biological activity. These proteins are essential for cellular remodeling events, including organelle biogenesis and vesicle trafficking. The actin cytoskeleton works in concert with membranes, both responding to curvature cues and helping to generate local deformation through polymerization or motor activity. This interplay allows membrane shape to guide signaling and cytoskeletal dynamics, creating feedback loops that maintain compartment integrity and spatial organization (Fletcher and Mullins, 2010).

Beyond basic cellular organization, the regulation of membrane curvature has direct relevance to human disease. Mutations in curvature-sensing proteins such as endophilin, dynamin, or reticulon family members are associated with neurodegenerative disorders, hereditary spastic paraplegia, and cancer (Montenegro et al., 2012; Alecu and Bennett, 2019). Viral entry and replication also depend on precise membrane remodeling events, many of which exploit curvature-sensing pathways (Mercer and Helenius, 2010). These pathological associations underscore the importance of understanding not only how membrane curvature is generated and maintained but also how cells use curvature as an informational cue to spatially and temporally control biological activity.

This recognition of curvature as a regulatory element has led to growing interest in the molecular sensors that interpret membrane shape. One well-studied class of such elements is curvature-sensing amphipathic motifs, which are short sequences that are intrinsically disordered in solution but form helices upon encountering curved membranes. These motifs have emerged as central players in the interpretation and generation of membrane curvature and are the subject of intense investigation (Drin and Antonny, 2010; Vanni et al., 2013).

1.2 Curvature-Sensing Mechanisms

Amphipathic helices are a widespread class of curvature-sensing elements. In solution, they lack defined structure, but they rapidly fold into helices on membrane surfaces. This folding behavior is driven by membrane-associated changes in lipid packing, which allow hydrophobic residues on one face of the helix to insert into the bilayer while polar or charged residues remain exposed to the cytosol (Cornell and Taneva, 2006; Kaiser and Kezdy, 1983). Because these defects are more pronounced in highly curved regions, amphipathic helices preferentially bind to curved membranes (Hristova et al., 1999).

Biochemical studies using artificial membranes have laid the groundwork for understanding how amphipathic motifs engage with curvature. Liposome-binding assays and synthetic bilayer systems have revealed that membrane association is enhanced by curvature, lipid disorder, and bilayer stress. However, these simplified environments often fail to mimic the biochemical heterogeneity of living cells. In particular, they do not reflect the influence of electrostatic gradients, lipid asymmetry, or crowding by other proteins, all of which may shape membrane binding in vivo.

Amphipathic motifs vary significantly in their curvature sensitivity and membrane selectivity. One class, known as Amphipathic Lipid Packing Sensor (ALPS) motifs, recognizes loose lipid packing. These motifs are enriched in small, uncharged polar residues and show high selectivity for curved membranes under in vitro conditions (Drin et al., 2007). One of ALPS motifs have been particularly well characterized is Golgi-associated proteins ArfGAP1, which localizes to highly curved Golgi membranes in reconstituted systems. However, this curvature selectivity is highly dependent on experimental conditions, including lipid composition and membrane tension. In fact, ArfGAP1's behavior has been shown to change significantly with the addition of charged lipids or in the presence of regulatory proteins, suggesting that its curvature-dependent localization may be modulated or even overridden in vivo.

Although amphipathic motifs share a common mechanism of folding upon membrane engagement, their functional specificity can vary widely. This variation likely arises from subtle differences in sequence composition, motif length, and helical stability, as well as from factors such as posttranslational modifications or domain context. As the field shifts toward understanding curvature sensing in cells, it becomes clear that simplified models must be supplemented by in vivo experiments that capture the full complexity of membrane environments. Studying curvature-sensing motifs in isolation or within minimal systems may obscure context-specific behavior that is central to their biological function.

1.3 Biophysical and Biochemical Principles Governing Curvature Sensitivity

The folding and membrane insertion of amphipathic motifs are key steps in curvature recognition. Highly curved membranes present more frequent lipid packing defects, which lower the energetic barrier for insertion. Motifs that fold efficiently into stable helices tend to bind membranes with greater specificity (Drin and Antonny, 2010; Jensen et al., 2011). Sequence composition strongly influences this process. Nonpolar faces rich in leucine, isoleucine, or tryptophan enhance insertion. Polar faces enriched in serine or threonine, as seen in ALPS motifs, favor binding to disordered, curved membranes (Drin et al., 2007; Vanni et al., 2013). Motifs with charged residues may show broader membrane affinity, depending on electrostatic interactions (Cui et al., 2011).

Helical length and flexibility also shape membrane engagement. Shorter helices may adapt dynamically to curvature, whereas longer ones stabilize interactions through sustained insertion (Braun et

al., 2017). Membrane tension further modulates curvature sensitivity by influencing lipid order. Post-translational modifications, such as phosphorylation, can reprogram motif activity by altering charge distribution or conformation (Kaneko et al., 2005).

Biophysical studies have employed reconstitution assays, fluorescence imaging, and molecular dynamics simulations to dissect these mechanisms. Liposome-binding assays reveal curvature preferences; supported bilayers and GUVs allow visualization of motif recruitment (Gudheti et al., 2007); and simulations provide atomic-level insights into folding and insertion (Sodt and Pastor, 2014). Together, these findings have clarified the energetic and structural basis for curvature sensitivity; however, more studies are needed to investigate how these in vitro findings of curvature-sensing apply in an active dynamic in vivo environment.

1.4 Functional Specificity of Curvature-Sensing Motifs of Endophilin A1

Endophilin A1 exemplifies how curvature-sensing motifs function within biologically essential processes. Its activity depends on a short amphipathic helix near the N-terminus (referred to as the H0 motif), a BAR domain that dimerizes to form a banana-shaped scaffold, and a C-terminal SH3 domain that recruits binding partners. Among these, the amphipathic H0 motif is necessary for membrane binding and curvature sensing (Weissenhorn, 2005; Gallop et al., 2006; Cestra et al., 1999). The H0 motif folds into an amphipathic helix upon encountering curved, negatively charged membranes. Its hydrophobic residues insert shallowly into the outer leaflet, while basic residues on the polar face interact with the membrane surface. Deletion of the H0 motif abolishes Endophilin's membrane association and disrupts its function in vesicle recycling, indicating that this short sequence is essential for coupling membrane curvature with biological activity (Boucrot et al., 2015; Bai et al., 2010).

Endophilin does not simply sense curvature, but it also promotes membrane remodeling. The H0 motif contributes to curvature generation by inserting into lipid packing defects, while the BAR domain oligomerizes to reinforce membrane bending. Together, these domains enable Endophilin to facilitate budding and fission of synaptic vesicles. Additional regulation comes from phosphorylation near the H0 motif, which can tune membrane affinity and timing of recruitment (Kaneko et al., 2005).

Because Endophilin integrates a structurally minimal curvature sensor with membrane-remodeling and signaling domains, it serves as a powerful model for dissecting the functional contributions of amphipathic helices. The modular design of Endophilin allows for systematic modification of its curvature-sensing elements, enabling researchers to probe the sequence determinants of functional specificity. As one of well-studied curvature-sensing proteins, Endophilin stands out as a excellent template for understanding how short helical motifs translate membrane features into biological outcomes.

Despite extensive efforts to characterize amphipathic motifs in vitro, the mechanisms by which these elements achieve functional specificity in vivo remain poorly defined. Although many amphipathic sequences associate with curved membranes in reconstituted systems, their localization and activity in cells are influenced by additional contextual factors that are often absent from simplified assays. It is not well understood how individual motifs target specific membrane compartments or trafficking pathways, nor how their sequence composition translates into functionally distinct behaviors within the cell.

Studies have suggested that amphipathic helices are embedded within multi-domain architectures that can influence their accessibility, membrane affinity, or response to regulatory inputs. In this setting, it is possible that the activity of a given motif is shaped not only by its intrinsic properties but also by domain context and local biochemical cues. In addition, post-translational modifications and lipid composition are thought to affect membrane-binding behavior of amphipathic motifs, but how these factors modulate curvature sensing under physiological conditions remains unclear (Drin and Antonny, 2010).

Defects in curvature-sensing machinery have been implicated in a range of human diseases, including neurodegeneration, oncogenic progression, and viral infection (Mercer and Helenius, 2010; Montenegro et al., 2012; Alecu and Bennett, 2019). Elucidating how amphipathic motifs contribute to membrane remodeling in vivo could therefore yield new molecular targets for therapeutic intervention. Our study aims to define the sequence features and biochemical requirements that govern the functional specificity of curvature-sensing motifs. By combining targeted mutagenesis, in vivo assays, and biophysical analysis, we seek to determine how structural variation within amphipathic helices influences

their activity in a cellular context. Focusing on the Endophilin H0 motif to uncover generalizable principles that link motif architecture to functional outcomes.

Chapter 2. The endophilin curvature-sensitive motif requires electrostatic guidance to recycle synaptic vesicles *in vivo*

Lin Zhang[1,†], Yu Wang[1,2,3,†], Yongming Dong[1], Aaradhya Pant[1], Yan Liu[1], Laura Masserman[1], Ye Xu[1], Richard N McLaughlin Jr[4], Jihong Bai[1,#]

[1] Basic Sciences Division, Fred Hutchinson Cancer Research Center, Seattle, WA 98109

[2] School of Life Sciences, Westlake University, Hangzhou, Zhejiang, P. R. China, 310024

[3] Fudan University, Shanghai, P. R. China, 200433

[4] Pacific Northwest Research Institute, Seattle, WA 98122

[†] These authors contributed equally to this work

[#] Jihong Bai, Ph.D. (Lead Contact and corresponding author)

Basic Sciences Division

Fred Hutchinson Cancer Research Center

1100 Fairview Ave N.

Seattle, WA 98109, USA

Email: jbai@fredhutch.org

2.1 Summary

Curvature-sensing mechanisms assist proteins in executing particular actions on various membrane organelles. Here, we investigated the functional specificity of curvature-sensing amphipathic motifs in *Caenorhabditis elegans* through the study of endophilin, an endocytic protein for synaptic vesicle recycling. We generated chimeric endophilin proteins by replacing the endophilin amphipathic motif H0 with other curvature-sensing amphipathic motifs. We found that the role of amphipathic motifs cannot simply be extrapolated from the identity of their parental proteins. For example, the amphipathic motif of the nuclear pore complex protein NUP133 functionally replaced the synaptic role of endophilin H0. Interestingly, non-functional endophilin chimeras had similar defects – producing fewer synaptic vesicles but more endosomes – indicating that the curvature-sensing motifs in these chimeras have a common deficiency at reforming synaptic vesicles. Finally, we converted non-functional endophilin chimeras into functional proteins by changing the cationic property of amphipathic motifs, successfully reprogramming the functional specificity of curvature-sensing motifs *in vivo*.

2.2 Introduction

Eukaryotic cells manage a network of membrane organelles that perform specific functions. Research on curvature-sensing mechanisms has intensified in recent years, as these principles show promise in coupling membrane morphology to biological activities (Antonny, 2011, Jarsch et al., 2016, McMahon and Gallop, 2005, Shibata et al., 2009, Prinz and Hinshaw, 2009). Such efforts have led to the identification of many curvature-sensing domains and motifs in proteins with various cellular functions, raising a possibility that curvature-sensing mechanisms assist proteins to perform specific activities on distinct membrane organelles. Yet, how exactly these mechanisms provide specific guidance to proteins *in vivo* remains largely unknown.

One class of curvature-sensing modules consists of amphipathic motifs — short membrane-binding sequences found in many proteins and peptides (Drin and Antonny, 2010, Shibata et al., 2009, Jarsch et al., 2016, Gimenez-Andres et al., 2018, Bigay and Antonny, 2012). In solution, the amphipathic motifs are disordered. Upon contact with curved membranes, they fold into a helical structure with polar and nonpolar residues segregated into two faces of the helix (Kaiser and Kezdy, 1983, Kaiser and Kezdy,

1984, Sargent et al., 1988, Cornell and Taneva, 2006). The amphipathic helices lay parallel onto membranes with residues in the nonpolar face embedded within the membrane hydrophobic core, and residues in the polar face oriented towards the aqueous cytoplasm and lipid headgroups (Hristova et al., 1999). The hydrophobic residues in the nonpolar face recognize lipid packing defects of curved membranes, consequently enabling curvature-dependent binding of amphipathic motifs to membranes (Vanni et al., 2013, Gonzalez-Rubio et al., 2011, Bartels et al., 2010, Cui et al., 2011, Hatzakis et al., 2009).

Previous biochemical studies found a number of factors influencing the curvature sensitivity of these motifs *in vitro*. The composition of amino acid residues in the polar face, for instance, has a strong impact on curvature sensitivity. The Amphipathic-Lipid-Packing-Sensor (ALPS) motifs, which have polar faces that mainly contain serine and threonine residues, are highly sensitive to membrane curvature (Drin et al., 2007, Drin and Antonny, 2010). In comparison, amphipathic motifs with polar faces abundant in basic residues, thus able to bind anionic membranes through electrostatic interactions, are thought to be less selective to curvature (Drin et al., 2007). Besides hydrophilic and charged residues in the polar face, the curvature-dependent membrane interactions of amphipathic motifs could be tuned by a number of additional parameters including size and density of hydrophobic residues in the nonpolar face (Bigay et al., 2005, Farsad et al., 2001, Krauss et al., 2008, Lee et al., 2005, Gallop et al., 2006, Masuda et al., 2006, Boucrot et al., 2012, Ford et al., 2002, Suresh and Edwardson, 2010), length of the amphipathic motifs (Copic et al., 2018, McLean et al., 1991, Braun et al., 2017), surrounding protein backbones (Doucet et al., 2015), and posttranslational modifications (Karanasios et al., 2010). These findings show a high degree of biochemical distinctions among amphipathic motifs, suggesting they could be further sorted into subgroups *in vitro* (Gimenez-Andres et al., 2018). However, little is known about the level of functional specificity these motifs display *in vivo*.

Endophilin-A (hereafter endophilin) is one of the best characterized endocytic proteins in neurons (Bai et al., 2010, Dickman et al., 2005, Kroll et al., 2019, Milosevic et al., 2011, Schuske et al., 2003, Verstreken et al., 2002, Watanabe et al., 2018, Kittelmann et al., 2013) and non-neuronal cells (Boucrot et al., 2015, Renard et al., 2015, Renard et al., 2020, Poudel et al., 2018, Ferreira and Boucrot, 2018). It harbors an amphipathic motif H0 at its N-terminus, a Bin-Amphiphysin-Rvs (BAR) domain in the middle,

and an SH3 domain at its C-terminus (Weissenhorn, 2005, Ringstad et al., 1997, Gallop et al., 2006, Peter et al., 2004, Farsad et al., 2001). Removal of endophilin from neurons leads to profound synaptic defects (Bai et al., 2010, Dickman et al., 2005, Kroll et al., 2019, Milosevic et al., 2011, Schuske et al., 2003, Verstreken et al., 2002, Watanabe et al., 2018, Kittelmann et al., 2013). The importance of endophilin H0 for supporting endocytosis is well established. Truncated endophilin that lacks the H0 motif folds correctly (Poudel et al., 2016, Cui et al., 2013) but fails to sustain synaptic vesicle (SV) recycling in neurons (Bai et al., 2010) and loses the ability to promote endocytic uptake of membranes in non-neuronal cells (Boucrot et al., 2015). Like other amphipathic motifs, endophilin H0 is disordered in solution (Low et al., 2008, Gallop et al., 2006, Bhatia et al., 2009). It folds rapidly into an amphipathic helix on membranes containing anionic lipids (Poudel et al., 2016, Capraro et al., 2013), with nonpolar residue side chains penetrating into the lipid bilayer (Jao et al., 2010, Cui et al., 2011). Because of the functional importance of the H0 motif, extensive effort has been put forward to elucidate the biochemical and biophysical basis for the interactions between endophilin H0 and membranes (Ambroso et al., 2014, Boucrot et al., 2012, Capraro et al., 2013, Chen et al., 2016b, Cui et al., 2013, Blood et al., 2008, Cui et al., 2011, Low et al., 2008, Bhatia et al., 2009, Hatzakis et al., 2009, Poudel et al., 2016). It is generally agreed that the H0 motif possesses the curvature-sensing activity essential for endophilin to bind curved membranes. H0 assists endophilin in generating membrane curvature by actively bending membranes (Low et al., 2008, Sodt and Pastor, 2014, Campelo et al., 2008, Poudel et al., 2016), passively stabilizing lipid packing defects presented on bent membranes (Hatzakis et al., 2009, Bhatia et al., 2009, Chen et al., 2016b, Poudel et al., 2016, Cui et al., 2011), or enhancing steric repulsion arising from protein crowding on membranes (Stachowiak et al., 2012, Chen et al., 2016a). Additionally, the activity of endophilin H0 can be tuned by phosphorylation (Kaneko et al., 2005) and interaction with the SH3 domain of endophilin (Vazquez et al., 2013, Wang et al., 2008, Chen et al., 2014)— both modulatory mechanisms requiring specific protein sequences. Collectively, these studies suggest that the H0 motif is a special amphipathic motif necessary for the activity of endophilin *in vitro*.

In this study, we generated endophilin chimeras by replacing endophilin H0 with other curvature-sensing amphipathic helical motifs. We found that only a subset of amphipathic motifs could support endophilin's synaptic activity in neurons, demonstrating functional specificity among amphipathic motifs *in*

vivo. We show that the specificity of an amphipathic motif cannot be simply extrapolated from the function of its parental protein. Interestingly, several endophilin chimeras carrying curvature-sensing motifs induce the abnormal accumulation of endosome-like structures at synapses, suggesting a common defect in the process of resolving endosomes into SVs. Finally, we successfully converted non-functional endophilin chimeras into functional ones by changing the cationic property of the amphipathic motifs. This study demonstrated how electrostatic and curvature-sensing mechanisms of H0 work together to provide specific guidance to endophilin function *in vivo*.

2.3 Results

2.3.1 The linker region between rEndoA1 H0 and the BAR domain tolerates changes.

In support of a conserved function of endophilin in invertebrate and vertebrate neurons, we found that neuronal expression of the GFP-tagged full-length rat endophilin A1 (rEndoA1, Fig.1A), using a single-copy transgene (*snb-1p::rEndoA1::gfp*), fully restored the locomotion rates (Fig.1B) and synaptic currents at neuromuscular junctions in *unc-57 endophilin null* mutant worms (Fig.1C-D). However, removal of the H0 motif from rEndoA1 (ΔH0) completely abolished the rescue activity of rEndoA1 in *unc-57* mutants (Fig.1B-D).

To understand how the N-terminal amphipathic helix H0 works in the context of full-length endophilin, we examined the linker region between H0 and the BAR domain. In wild type rEndoA1, this is a short GlyGlyAla linker (Fig.1A), suggesting a flexible connection. To determine whether a particular length of amino acid residues is required, we generated mutant versions of rEndoA1 carrying additional residues of Gly, GlyGly, and GlyGlyAla before the BAR domain (indicated by the arrow in Fig.1A). Our data showed that mutant rEndoA1 with altered linkers exhibited similar levels of the rescue activity in restoring locomotion rates (Fig.1B), the frequency of endogenous excitatory postsynaptic currents (EPSCs) (Fig.1C), and the amplitude of evoked EPSCs in response to electrical stimulation (Fig.1D), indicating that the flexible linker connecting the amphipathic helix H0 to the rEndoA1 BAR domain can tolerate changes associated with sequence elongation.

2.3.2 Endophilin H0 carries functional specificity in vivo.

We next sought to examine the functional specificity of endophilin H0 *in vivo*. We generated an array of rEndoA1 chimeras carrying amphipathic motifs from various proteins in place of endophilin H0 (Fig. 2A-B). The amphipathic motifs grafted into these endophilin chimeras have different primary sequences but are all known curvature sensors as shown by biochemical studies, *i.e.*, they preferentially bind highly curved membranes *in vitro* (Drin and Antonny, 2010). The rEndoA1 chimeras were expressed in neurons using single-copy transgenes, and expression levels were measured by determining the GFP fluorescence intensity around the *C. elegans* nerve ring (a tight bundle of neuronal processes of sensory and interneurons). Imaging results showed that rEndoA1 chimeras were expressed in neurons at similar levels to wild type rEndoA1 (Figure S1A).

To determine whether the function of endophilin H0 *in vivo* could be replaced by other curvature-sensing amphipathic motifs, we examined locomotion rates of transgenic *unc-57 endophilin* mutant worms expressing various rEndoA1 chimeras (Fig.2C-D). Several of these rEndoA1 chimeras significantly recovered the locomotion defects in *unc-57 endophilin* mutants. Among these, amphipathic motifs from BIN1 (Bridging Integrator 1, also known as Amphiphysin-2; (Low et al., 2008)), NUP133 (Nucleoporin 133 (Doucet et al., 2010)), and Nadrin2 (Rho GTPase activating protein 17; (Galic et al., 2012)) significantly restored rEndoA1 H0 function. And yet other amphipathic motifs, including those from SV binding proteins (*e.g.*, complexin CPX-1 (Snead et al., 2014, Wragg et al., 2013), α-Synuclein (Jao et al., 2008, Davidson et al., 1998, Georgieva et al., 2008)) , intracellular membrane trafficking (*e.g.,* ARF1 (Goldberg, 1998), KES1 (Im et al., 2005, Moser von Filseck et al., 2015), and Sar1p (Lee et al., 2005)), either failed or had only low activity in substituting rEndoA1 *in vivo*. These results demonstrate that endophilin H0 could carry a level of functional specificity shared only by a subset of curvature-sensing amphipathic motifs. Interestingly, such functional specificity could not be extrapolated from the cellular activity or localization of the parent proteins. For example, NUP133 functions at nuclear pores (Nordeen et al., 2020, Lutzmann et al., 2002, Doucet et al., 2010), but its amphipathic motif could replace the function of rEndoA1 H0 at synapses. Additional mechanisms, beyond sensing membrane curvature, may need to be engaged for defining *in vivo* specificity of amphipathic motifs.

2.3.3 Two ALPS motifs show drastic differences in their ability to replace rEndoA1 H0 at synapses.

To understand the functional specificity of amphipathic motifs, we focused on two chimeric proteins: NUP133_rEndoA1 and KES1_rEndoA1. Biochemical studies have shown that the amphipathic motifs of NUP133 and KES1 act in a similar way to sense membrane curvature *in vitro*; they are now recognized as two founding members of the family of ALPS motifs (Drin et al., 2007). Despite the biochemical similarity, NUP133 and KES1 ALPS motifs exhibited drastic differences in their ability to replace rEndoA1 H0 *in vivo*. Expression of NUP133_rEndoA1 in *unc-57 endophilin* mutants significantly improved locomotion rates. By contrast, worms carrying the KES1_rEndoA1 chimera moved much slower than the NUP133_rEndoA1 worms (Fig.2D).

One possible reason for the functional deficiency of KES1_rEndoA1 was that this chimeric protein failed to localize to synapses. To examine this possibility, we compared the synaptic and axonal distribution of the proteins rEndoA1 wild type (wt), the H0-truncated mutant (ΔH0), NUP133_rEndoA1, and KES1_rEndoA1, which were all tagged with mScarlet (a red fluorescent protein) (Fig.2E). We found that, similarly to wild type rEndoA1 and NUP133_rEndoA1, KES1_rEndoA1 colocalized with the presynaptic marker GFP::RAB-3 (Figure S1B). Quantification of the fluorescence images showed that the synaptic and axonal distributions of both NUP133_rEndoA1 and KES1_rEndoA1 proteins were identical to that of wild type rEndoA1 (Fig.2E). These data show that the KES1_rEndoA1 was trafficked to synapses and enriched there, yet could not fully replace the function of endophilin. Therefore, mechanisms other than protein-trafficking defects are needed to explain the functional difference between NUP133_rEndoA1 and KES1_rEndoA1.

To define the synaptic activity of NUP133_rEndoA1 and KES1_rEndoA1, we examined the levels of synaptic transmission using electrophysiological recordings. Due to their endocytosis defects, *unc-57 endophilin* mutants have a smaller pool of SVs and a corresponding decrease in synaptic transmission (Bai et al., 2010, Kittelmann et al., 2013, Schuske et al., 2003). Specifically, *unc-57 endophilin* mutants had a decreased rate of endogenous EPSCs at neuromuscular junctions, while the mean amplitude of endogenous EPSCs was not altered (Fig.3A). The amplitude of evoked EPSCs in *unc-57* mutants was also significantly reduced (Fig.3B). These synaptic transmission defects in *unc-57 endophilin* mutants

were fully rescued upon expression of chimeric NUP133_rEndoA1 (Fig.3A), demonstrating a functional similarity between the NUP133 ALPS motif and rEndoA1 H0. In comparison, KES1_rEndoA1 showed only partial activity for improving synaptic transmission in *unc-57 endophilin* mutants (Fig.3A-B). These results demonstrate that for sustaining synaptic transmission *in vivo*, the NUP133 ALPS is a more efficient substitute for the role of endophilin H0 than the KES1 ALPS.

To determine the impact of NUP133_rEndoA1 and KES1_rEndoA1 on SV recycling, we used imaging analysis to follow the release and retrieval of SVs from the glutamatergic neuron ASH in intact worms (Ventimiglia and Bargmann, 2017). As shown in Fig.3C, a pH-sensitive GFP (super-ecliptic pHluorin) was inserted into the first lumenal domain of the vesicular glutamate transporter EAT-4 (VGLUT), resulting in a fluorescent VGLUT-pHluorin reporter. At the resting state, VGLUT-pHluorin fluorescence was quenched by the acidic pH of the vesicle lumen. SV exocytosis delivered VGLUT-pHluorin to the plasma membrane, resulting in an increase of green fluorescence due to de-quenching of pHluorin at neutral extracellular pH. Subsequently, endocytosis and reacidification took place, returning VGLUT-pHluorin back to the quenched state. As expected, *unc-57 endophilin* mutants had significantly slowed VGLUT-pHluorin retrieval after stimulus removal (Fig.3D and 3F left panel), showing that the speed of SV recycling is impaired in neurons lacking endophilin. In addition, baseline VGLUT-pHluorin fluorescence in the ASH neuron was higher in *unc-57 endophilin* mutants than in wild type worms (Fig.3F right panel), indicating that an elevated level of VGLUT-pHluorin remained on the cell surface at steady-state. Expression of NUP133_rEndoA1 fully recovered the retrieval rates (Fig.3E left panel, Fig.3F left panel) and the basal levels (Fig.3F right panel) of surface VGLUT-pHluorin in *unc-57* mutants. In contrast, expression of KES1_rEndoA1 failed to significantly accelerate the VGLUT-pHluorin retrieval (Fig.3E right panel, Fig.3F left panel). However, the basal level of surface VGLUT-pHluorin at KES1_rEndoA1 synapses did return to the wild-type level (Fig.3F right panel). Next, we applied Bafilomycin A1 to inhibit the V-ATPase that drives the acidification of intracellular compartments. We found that the basal fluorescence intensity of VGLUT-pHluorin was significantly increased at KES1_rEndoA1 synapses upon blocking V-ATPase-dependent luminal acidification (Figure S1C). Together, these data suggest that the recycling of SV proteins is slowed but not abolished at KES1_rEndoA1 synapses.

2.3.4 Synapses rescued by the KES1_rEndo chimera have abnormal endosome-like structures.

To better understand the deficiency of KES1_rEndoA1, we performed high-pressure freeze electron microscopy to examine synapses at the ultrastructural level (Fig.4A) and identified several abnormal features at KES1_rEndoA1 synapses. First, the abundance of SVs was only partially restored in transgenic *unc-57 endophilin* mutants that carried KES1_rEndoA1 (Fig.4A, 4B left panel). Second, more large clear vesicles (50-100 nm diameter) appeared at KES1_rEndoA1 synapses (Fig.4C left panel), and SVs (Fig.4B right panel) and large clear vesicles (Fig.4C right panel) were also larger at KES1_rEndoA1 synapses than those in wild type or *unc-57* mutant synapses. Because the amplitude of endogenous EPSCs remained unchanged at KES1_rEndoA1 synapses, the enlarged vesicles were likely deficient at releasing neurotransmitters. Third, we found a significant increase in the number of endosome-like structures (>100 nm in diameter) at KES1_rEndoA1 synapses (Fig.4D left panel). The endosome-like structures occurred more frequently at KES1_rEndoA1 synapses (16 out of 18) than at *unc-57* mutant synapses (9 out 25; Fig.4D right panel). Because our results showed that KES1_rEndoA1 synapses had fewer SVs but more endosome-like structures, we examined the possibility that endosome-like structures and SVs compete for membranes. We found an inverse correlation between SV abundance and size of endosome-like structures at synapse (Fig.4E), supporting a competitive nature between these two distinct types of membrane organelles. Finally, to determine whether SV exocytosis provides the membranes for the endosome-like structures, we introduced the *unc-64(e246) syntaxin1* mutation to reduce the level of SV exocytosis. The frequency of endosome-like structures was significantly reduced at KES1_rEndoA1 synapses in *unc-57, unc-64* double mutants (Fig.4F, 0 out of 12 synapses). These data indicate that the formation of endosome-like structures at KES1_rEndoA1 synapses requires the exocytosis of synaptic vesicles.

Next, we sought to determine factors that limit the ability of the KES1 ALPS motif to replace endophilin H0. We first looked into biochemical differences among endophilin H0, NUP133 ALPS, and KES1 ALPS motifs. It was previously suggested that the abundance of basic residues is a major factor differentiating endophilin H0 from members in the ALPS family (Drin et al., 2007, Drin and Antonny, 2010). Interestingly, while the ALPS motifs of NUP133 and KES1 both belong to the ALPS family (Drin et

al., 2007), they have different cationic levels. The KES1 ALPS motif has a net charge level of 0, and the NUP133 ALPS motif has a net charge level of +2, whereas rEndoA1 H0 has a net charge level of +4 (Figure S2A). Alignment of amphipathic helix sequences showed that the net charge levels of KES1, NUP133, and rEndoA1 motifs remained largely constant across orthologs from various species (Figure S2B), suggesting that the levels of positive charges of these motifs are preserved during evolution.

2.3.5 The charge level of KES1_ALPS limits its potential to substitute endophilin H0 in vitro.

To determine how grafted amphipathic motifs influence chimeric rEndoA1, we used electron microscopy to study the ability of chimeric rEndoA1 to generate membrane tubules. Previous studies showed that membrane tubulation activity of wild type endophilin requires interactions with lipids of negatively charged headgroups (*e.g.*, phosphatidylserine PS and phosphatidylinositol 4,5-bisphosphate PIP2) (Farsad et al., 2001, Gallop et al., 2006, Jao et al., 2004, Masuda et al., 2006). Consistent with these early findings, our control experiments showed that wild type rEndoA1 generated more, and longer, membrane tubules on liposomes with correspondingly increased amounts of negatively charged lipids (Figure S3A-B). We then compared NUP133_rEndoA1 and wild type rEndoA1, which generated identical amounts of membrane tubules on liposomes (Figure S3C-D). By contrast, the KES1_rEndoA1 chimera failed to produce abundant membrane tubules on liposomes carrying either 15%PS/85%PC or 25%PS/0.5%PIP2/74.5%PC (Figure S3C-D). The reduction in membrane tubulation by KES1_rEndoA1 was likely due to changes of electrostatic sensing, rather than membrane tubulation capability *per se*, because KES1_rEndoA1 robustly produced membrane tubules when membrane PIP2 was increased to 2% (Figure S3D). Thus, KES1_rEndoA1 requires a higher amount of negatively charged lipids to tubulate liposomes (PIP2 bears four negative charges whereas PS has one), raising a possibility that the net charge level of 0 of KES1 ALPS limits the potential of this motif to substitute endophilin H0.

2.3.6 Increasing net positive charges of the KES1 ALPS motif improves its synaptic function.

To define the relationship between charge distribution and functionality of amphipathic motifs, we engineered mutations to improve the function of the KES1_rEndoA1 chimera *in vivo*. If the net charge

level was indeed a limiting factor, introducing positive charges into the KES1 ALPS should improve its functionality. As a member of the ALPS family, the amphipathic motif of KES1 is rich in hydrophilic residues such as serine (S) and threonine (T). To add positive charges to the KES1 ALPS motif, we introduced mutations to convert hydrophilic S/T residues into positively charged lysine (K) residues. We generated single K mutations to S2, S3, and S4 — three residues in the first turn of the KES1 amphipathic helix (Fig.5A). These single mutations (S2K, S3K, or S4K) significantly improved the activity of KES1_rEndoA1 to restore locomotion rates in *unc-57 endophilin* mutants (Fig.5B-C). Interestingly, S2K, S3K, or S4K mutations led to a similar level of locomotory improvement, suggesting that the position of these mutations had little or no impact on the functional changes of mutant KES1_rEndoA1. Indeed, when we systematically introduced single K mutations to change each S/T site in the KES1 motif, every single S/K mutant protein partially, but significantly, restored locomotion activity, with similar locomotion rates among the KES1_rEndoA1 S/K mutant worms, regardless of the position of the mutation (Fig.5C). These data suggest that the S/K mutations improved KES1_rEndoA1 function by increasing the net positive charge rather than by altering specific charge locations.

Since single S/K mutations only partially restored the locomotion activity, we asked whether addition of a second K residue, bringing the net charge from +1 to +2, would further improve the activity of KES1_rEndoA1 *in vivo*. Indeed, a combination of two single S/K mutations (S4K and S20K) showed significantly enhanced activity in restoring locomotion of *unc-57 endophilin* mutant worms, when compared to the single S4K and S20K mutants (Fig.5B and 5C). Next, we determined the impact of S4K,S20K KES1_rEndoA1 at synapses using both functional and ultrastructural analyses. First, electrophysiological recordings showed that expression of S4K,S20K KES1_rEndoA1 fully restored the amplitude of evoked EPSCs (Fig.5D), and the frequency of endogenous EPSCs (Figure S4) in *unc-57 endophilin* mutants. Second, we found that VGLUT-pHluorin retrieval at synapses was fully recovered by expression of S4K,S20K KES1_rEndoA1 in *unc-57 endophilin* mutants (Fig.5E). Third, electron microscopy results showed that the abundance of SVs at S4K,S20K KES1_rEndoA1 synapses was recovered to a level close to that in wild type synapses (Fig.5F-G). Further, the number of endosome-like structures was significantly reduced when compared to synapses carrying KES1_rEndoA1 (Fig.5H). Together, these findings demonstrate that increasing the net charge to +2 improved the activity of

KES1_rEndoA1 enough to substitute endophilin H0, and enabled mutant KES1_rEndoA1 to efficiently support synaptic activities.

2.3.7 The synaptic function of DivIVA_rEndoA1 is improved by introducing positive net charges into its curvature-sensing motif.

To determine how other amphipathic motifs respond to changes of net charge level, we investigated the sequence from DivIVA, a bacterial protein involved in cell division (Hempel et al., 2008, Lenarcic et al., 2009). The DivIVA amphipathic motif shares some similar properties with the KES1 ALPS motif. First, expression of the DivIVA_rEndoA1 chimeric protein failed to restore locomotion activity in *unc-57 endophilin* mutant worms (Fig.2C and 2D). Second, the net charge level of the DivIVA amphipathic motif is 0 (Fig.6A), which is identical to that of KES1 ALPS. However, unlike KES1 ALPS, which lacks a significant amount of charged residues, the DivIVA amphipathic motif has 3 positive charges (from Lys and Arg) and 3 negative charges (from Asp and Glu), resulting in a net charge of 0 (Fig.6A). This unique electrostatic property allowed us to alter the net charge level in another way. Instead of using K residues, we introduced E4S, D12S, and E14S mutations into the DivIVA amphipathic motif to bring the net charge level to +3. We then examined the *in vivo* function of the wild type (wt) and triple mutant (E4S,D12S,E14S) versions of DivIVA_rEndoA1 chimeras using behavioral, electrophysiological, imaging, and ultrastructural analyses. In contrast to the failure of restoring locomotion by wt_DivIVA_rEndoA1, expression of the triple mutant E4S,D12S,E14S_DivIVA_rEndoA1 chimera in *unc-57* mutant worms fully restored locomotion (Fig.6B), endogenous EPSCs (Fig.6C), and evoked EPSCs (Fig.6D), as well as retrieval rates and basal levels of VGLUT-pHluorin (Fig.6E). Ultrastructural data showed that expression of the wt_DivIVA_rEndoA1 chimera in *unc-57* mutant animals failed to recover the SV abundance and led to the formation of abnormal endosome-like structures at synapses (Fig.6F-H). In contrast, we found that at synapses carrying the E4S,D12S,E14S_DivIVA_ rEndoA1 chimera, the number of SVs was returned to a normal level, and no endosome-like structures were observed (Fig.6F-H). Together, these data present a second case where the function of endophilin chimeras could be improved *in vivo* by introducing positive net charges into a curvature-sensing motif.

2.3.8 The net positive charge of the H0 motif is essential for the function of endophilin at synapses.

Finally, we examined the electrostatic property of endophilin H0 and its role in supporting synaptic activity. The H0 motif of rEndoA1 has a net charge level of +4, with 5 positively charged Lys residues and 1 negatively charged Glu residue (Fig.7A). Alignment analysis showed that all Lys residues are highly conserved among orthologs of endophilin A1 across species (Figure S2B). To determine if conserved Lys residues are required, we introduced single K/S mutations to the rEndoA1 H0 motif and expressed mutant versions of rEndoA1 in *unc-57 endophilin* mutants. Interestingly, single K/S mutations had little impact on the rescue activity of rEndoA1 in restoring locomotion rates (Figure S5A), yet showed a clear additive effect of disrupting the function of endophilin, as locomotion rates became lower when combinations of more K/S mutations were added (Fig.7B). To understand how K/S mutations alter the function of endophilin at synapses, we performed electrophysiological recordings to determine the levels of synaptic transmission. Like the locomotion results, we found that increases in the number of K/S mutations led to slower rates of endogenous EPSCs (Fig.7C) and lower amplitudes of evoked EPSCs (Fig.7D), without affecting the amplitudes of endogenous EPSCs (Figure S5B). In particular, the introduction of 4 K/S mutations (K7S,K8S,K16S,K20S) completely abolished the ability of rEndoA1 to restore synaptic currents, indicating that positively charged Lys residues function as a collective group even though the highly conserved individual lysine residues are not essential. Interestingly, our ultrastructural analysis showed that synapses carrying the 4 K/S mutant rEndoA1 had more endosome-like structures and fewer SVs (Fig.7E-G), resembling features of KES1_rEndoA1 synapses. These results show that the net positive charge of the H0 motif is essential for the function of endophilin at synapses, further supporting the conclusion that the level of net charge contributes to the functional specificity of curvature-sensing motifs *in vivo*.

2.4 Discussion

Amphipathic α-helical motifs are often found in proteins that regulate the trafficking of membrane organelles. These motifs are thought to carry out specific activities for assisting their parental proteins in performing distinct cellular functions. In recent years, *in vitro* studies using synthetic membranes and

molecular dynamics simulations have found a wealth of plausible mechanisms for interactions between amphipathic motifs and membranes. However, due to a lack of systematic analysis *in vivo*, understanding of these motifs is largely limited to working models. This study used a protein engineering approach to identify factors that are sufficient to define the specificity of amphipathic motifs *in vivo*. Our findings led to several conclusions on mechanisms governing the specificity of endophilin H0 in living neurons.

(i) The function of the H0 motif does not require a specific protein sequence. We found that unrelated amphipathic sequences can substitute endophilin H0 for synaptic function, uncoupling the essential function of the H0 motif from specific protein-protein interactions (*e.g.*, binding between endophilin H0 and SH3 domains (Chen et al., 2014, Vazquez et al., 2013, Wang et al., 2008)). In addition, the linker between H0 and the BAR domain of endophilin is flexible and tolerates sequence lengthening, indicating that H0 has structural freedom from the rest of the protein.

(ii) The specificity of an amphipathic motif cannot be simply extrapolated from the function of its parental protein; investigations that include functional studies are required. For instance, when grafted into endophilin, the amphipathic motif from the nuclear pore complex protein NUP133 (Nordeen et al., 2020, Lutzmann et al., 2002, Doucet et al., 2010) can replace the endophilin H0 motif in its role at synapses. Thus, amphipathic motifs could carry similar functions, even though their parental proteins may act on different membrane organelles.

(iii) Electrostatic contribution is key for amphipathic motifs to support the activity of endophilin at synapses. This electrostatic contribution appears to be independent to the location of charges or particular types of amino acid residues. Instead, the level of net charges modulates the activity of endophilin H0. Single K/S mutations in the endophilin H0 motif have little impact, but in combination disrupt endophilin's activity at synapses in an additive manner. It is worth noting that the importance of electrostatic property is perhaps not limited to the H0 motif of endophilin, as we found that K/S mutations in the endophilin HI amphipathic motif also exhibited an additive and disruptive effect on animal locomotion (Figure S6). These findings suggest that the two amphipathic motifs of endophilin follow the same principle - using the net positive charge of amphipathic motifs to guide the endophilin's function.

(iv) Endophilin H0 senses both curvature and electrostatic status of membranes. The amphipathic motifs of NUP133 and endophilin were previously categorized into two subgroups based on the type of

residues in the polar face – the NUP133 amphipathic motif is a *bona fide* curvature sensor in the ALPS motif family (Drin and Antonny, 2010, Drin et al., 2007) due to abundant polar serine and threonine residues, whereas endophilin H0 is thought to have low sensitivity to membrane curvature because it is rich in charged residues. In contrast to the anticipated distinction between two subgroups of amphipathic motifs, we found that NUP133 ALPS successfully replaced endophilin H0 *in vivo*. These results suggest that the functional boundary between ALPS motifs and endophilin H0 is not absolute. NUP133_ALPS and endophilin H0 likely play similar roles as dual sensors for membrane curvature and negatively charged lipids.

Other properties besides the electrostatic status could also contribute to the functional specificity *in vivo*. For instance, while two amphipathic motifs from ARF1 and Epsin1 are positively charged, they failed to substitute for the function of endophilin H0 (Fig.2D). We speculate that the short length of these amphipathic motifs could be a contributing factor, as changes of sequence length could alter binding properties with membranes (Copic et al., 2018, McLean et al., 1991, Braun et al., 2017). However, further studies are necessary to fully address this issue.

What is the contribution of positively charged residues in endophilin H0 to synaptic activity *in vivo*? We found that the cationic property of endophilin H0 has a strong impact on endosome-like structures, which could represent the intermediate membrane organelles that support the endocytic reformation of synaptic vesicles (SV) (Watanabe et al., 2013a, Watanabe et al., 2013b, Watanabe et al., 2014, Hoopmann et al., 2010, Kononenko and Haucke, 2015, Clayton and Cousin, 2009). In support of this view, disruption of SV exocytosis significantly reduced the abundance of endosome-like structures (Fig.4F), suggesting that the formation of endosome-like structures is coupled to the SV cycle. Recent studies show that, following the exocytosis of SVs, endophilin acts at two distinct sites to recycle SV proteins and membranes. It promotes endocytic retrieval from the plasma membrane into endosomes (Watanabe et al., 2018, Kononenko et al., 2014), and then helps to resolve endosomes into SVs (Watanabe et al., 2018, Kittelmann et al., 2013). This two-step model suggests that complete removal of endophilin from synapses would block the initial endocytic retrieval, imposing a negative impact on the formation of endosomes. Consistent with this, the probability of finding endosome-like structures at *endophilin* mutant synapses is low (Fig.4). By contrast, at synapses expressing endophilin chimeras with

few positive charges (*e.g.*, KES1_rEndoA1, DivIVA_rEndoA1 and rEndoA1 with 4 K/S mutations), endosome-like structures become abundant and are much more frequently observed (Fig.4, Fig.6H, and Fig.7G). Such endosomal changes are likely at the expense of SVs, there being a negative correlation between the size of endosome-like structures and the abundance of SVs (Fig.4E). Other mechanisms without a direct link to the SV cycle could also lead to endosome accumulation at synapses. Several studies show that endophilin has a critical role in regulating autophagosome formation at synapses by inducing membrane curvature to recruit autophagic machinery (Matta et al., 2012, Soukup et al., 2016, Murdoch et al., 2016, Yang et al., 2022). In particular, a phosphomimetic endophilin with altered electrostatic property of the HI helix can promote autophagosome formation at the *Drosophila* neuromuscular junctions (Soukup et al., 2016). The connection between endocytic machinery and autophagosome biogenesis is highly intriguing, as its misregulation contributes to early-onset Parkinsonism (Hill and Colon-Ramos, 2020, Soukup et al., 2018). Nonetheless, these findings show that endophilin requires a strong net positive charge in amphipathic motifs to regulate endosomes and SVs in neurons. Amphipathic motifs with sole activities in curvature-sensing (*e.g.*, KES1_ALPS) are not sufficient for endophilin to sustain a normal pool of SVs.

Results in this study provide *in vivo* evidence supporting a dual sensing capability of endophilin H0 to detect both curvature and electrostatic states of membranes. The cationic property of H0 is likely more important for the role of endophilin on endosomes than on the plasma membrane, because these membranes contain anionic lipids with distinct properties (Balla, 2013, Di Paolo and De Camilli, 2006). The plasma membrane is abundant with phosphatidylinositol 4,5-bisphosphates that bear a negative charge of ~4, whereas endosomes are enriched for phosphatidylinositol phosphates that have a negative charge of ~1.5. As a result, to recognize endosomal membranes, the endophilin H0 motif may require a high level of positive charges to reach sufficient electrostatic interactions. Future studies are needed to address this scenario in detail. Nonetheless, our studies demonstrate an electrostatic contribution for endophilin H0 to function *in vivo*. We propose a model in which the H0 motif carries a dual sensing activity of membrane curvature and electrostatic status to ensure endophilin's action at distinct sites during synaptic vesicle endocytosis.

Limitations of study – A future research direction for us is to examine the contribution of endophilin amphipathic motifs to presynaptic autophagosome biogenesis.

2.5 Acknowledgments

This research was supported by NIH R01GM127857 and R01NS115974 to JB. The authors thank the *Caenorhabditis elegans* Genetics Center (funded by NIH Office of Research Infrastructure Programs P40 OD010440) and Dr. Cori Bargmann for worm strains. We thank Dr. Susan Parkhurst for critical reading of the manuscript. Electron microscopy data were generated using the Fred Hutchinson Cancer Research Center Electron Microscopy Shared Resource (EMSR). The EMSR is supported in part by the Cancer Center Support Grant P30 CA015704-40.

Author contributions

J.B., L.Z., Y.W., and R.M.Jr designed the experiments. L.Z., Y.W., Y.D., A.P., Y.L., Y.X., and R.M.Jr performed experiments and analyzed data; J.B. supervised the study and wrote the manuscript with input from L.M. and R.M.Jr.

Declaration of interests

The authors declare no competing interests.

2.6 Figure Legends

Figure 1. The linker between the N-terminal amphipathic helix H0 and the BAR domain of endophilin tolerates changes.

(A) *Upper panel* - Schematic diagram showing the domain structure of rat Endophilin A1 (rEndoA1). The amino acid sequence of the N-terminal amphipathic helix H0 (residues 1-21) is shown in brown, followed by an endogenous flexible linker (GGA) that connects endophilin H0 to the BAR domain. The blue arrow indicates insertions of amino acid residues after the endogenous linker. *Lower panel* – A helical wheel presentation of rEndoA1_H0. Amino acid residues are colored as following; yellow, hydrophobic; blue, basic; red, acidic; purple, serine, threonine, asparagine, glutamine and histidine; grey, glycine; light yellow, alanine. A pan-neuronal promoter *snb-1p* was used to drive transgene expression. Single-copy transgenes *(snb-1p::rEndoA1::gfp)* encoding GFP-tagged rEndoA1 variants were introduced into *endophilin unc-57(e406)* mutant worms. **(B)** Locomotion data. Representative trajectories of 30s locomotion are shown for each genotype (15 animals). The starting points of locomotion recordings were aligned and indicated by red dots for clarity. The scale bar indicates 1 mm. Summary data for locomotion rates were shown in the bar graphs. For all figures thereafter (unless specified), the number of worms analyzed for each genotype was indicated in the bar graphs, and error bars represent standard error of the mean (SEM). **(C)** Representative traces and summary data for endogenous excitatory postsynaptic currents (EPSC) rates and amplitudes. **(D)** Evoked EPSC traces and summary data. ***, $p < 0.001$; when compared to *endophilin unc-57 mutants*. One-way ANOVA followed by Dunnett's test.

Figure 2. Endophilin chimera carrying amphipathic helices from various proteins displayed functional specificity *in vivo*.

(A) Schematic diagram showing the domain structure of chimeric versions of rEndoA1 (tagged with GFP at C-terminus). The H0 motif of rEndoA1 (colored in blue) was replaced by curvature-sensing amphipathic helices from various proteins. Helical wheel presentations of amphipathic helices used for generating endophilin chimera were shown in **(B)**. Amino acid residues were colored as described in the legend of Figure 1. Single-copy transgenes *(snb-1p::rEndoA1_chimera::gfp)* were introduced into *endophilin unc-*

57(e406) mutant worms to express GFP-tagged rEndoA1 chimera in neurons. **(C)** Representative trajectories of locomotion were presented as described in the legend of Figure 1B. **(D)** Summary data for locomotion rates. **(E)** The distribution of rEndoA1 proteins at synapses and in axons. Fluorescence analysis was done as previously described (Burbea et al., 2002, Bai et al., 2010, Dittman and Kaplan, 2006). Representative images and summary data were shown for indicated genotypes. ***, $p < 0.001$; when compared to rEndoA1 ΔH0. Scale bars: 2 μm.

Figure 3. The KES1_rEndoA1 chimera has reduced activity in supporting synaptic transmission and recycling synaptic vesicle proteins.

Single-copy transgenes that encode GFP-tagged KES1_rEndo and NUP133_rEndo were introduced into *endophilin unc-57(e406)* mutants. **(A)** Endogenous EPSC frequency and amplitude. **(B)** Evoked EPSC (eEPSC). **(C)** Schemes illustrating the analysis of VGLUT-pHluorin fluorescence in *C. elegans* sensory neurons (ASH) upon sensory stimulation (Ventimiglia and Bargmann, 2017). Transgenic worms expressing VGLUT-pHluorin in the sensory ASH neuron were challenged for 10 seconds by 0.5M NaCl ("stimulus ON"). Exocytosis of SVs triggered by NaCl stimulation delivers VGLUT-pHluorin to the plasma membrane, causing an increase in the pHluorin fluorescence in ASH neurons. After removal of NaCl stimuli ("stimulus OFF"), surface VGLUT-pHluorin was retrieved from the plasma membrane via endocytosis. Reacidification of SVs quenches the pHluorin fluorescence. Representative images of VGLUT-pHluorin acquired before, during, and after NaCl stimulation were shown in the insert. Scale bars: 2 μm. **(D)** VGLUT-pHluorin responses from wild type and *endophilin unc-57* mutant worms. Grey rectangles indicated "stimulation-on". Shading indicated SEM. **(E)** VGLUT-pHluorin responses from transgenic *unc-57* mutant worms carrying KES1_rEndo *(left; green)* and NUP133_rEndo *(right; blue)*. The VGLUT-pHluorin response from wild type synapses was shown for clarity. **(F)** Quantification of the recovery time constants *(left)* and the basal levels of VGLUT-pHluorin fluorescence *(right)*. ***, $p < 0.001$; when compared to *endophilin unc-57 mutants*. $^{###}$, $p < 0.001$ and $^{##}$, $p < 0.01$; when compared to KES1_rEndo chimera. The number of synapses analyzed for each genotype is indicated in the bar graphs.

Figure 4. Synapses rescued by the KES1_rEndo chimera have increased accumulation of abnormal endosome-like structures.

(A) Representative transmission electron micrographs of synapses in the ventral nerve cords of adult hermaphrodites. Yellow shading indicates dense projections (DP). White arrow heads indicate endosome like structures (EL; >100 nm in diameter). Scale bars indicate 100 nm. Quantification of the abundance of SVs (<50 nm in diameter) per synaptic profile (**B**, *left*) and large clear vesicles (LCV; 50-100 nm in diameter) per synaptic profile (**C**, *left*) were shown as mean ± standard error. The diameter of SVs (**B**, *right*) and LCVs (**C**, *right*) were presented as box-whisker plots. Whiskers indicate minimum and maximum values. Data were collected from 40 wild type, 40 *unc-57* mutant, 20 ΔH0_rEndoA1, and 31 KES1_rEndoA1 synaptic profiles. **(D)** The number of endosome-like structures (EL; >100 nm in diameter) per synapse was plotted as mean ± standard error (*left*). ***, $p < 0.001$; **, $p < 0.01$; n.s., not significant; The fraction of synapses with and without ELs was plotted for each genotype (*right*). Data were collected from 24 wild type, 25 *unc-57* mutant, 16 ΔH0_rEndoA1, and 18 KES1_rEndoA1 synapses. **(E)** A scatter plot illustrated the negative relationship between the size of ELs and the abundance of SVs. The y-axis value of each dot indicates the sum of maximum cross-sectional areas of endosome-like structures in a synapse. The corresponding x-axis value indicates the mean number of SVs per synaptic profile of the same synapse where the y-value was determined. Data obtained from KES1_rEndo synapses were colored in blue. The grey dot indicates data from wild type synapses (the mean number of SVs per profile and the lack of endosome-like structures). The purple line indicated the best fit of simple linear regression. $R^2 = 0.34$ and * $p < 0.05$. **(F)** The fraction of KES1_rEndoA1 synapses with and without endosome-like structures in *unc-57(e406)* single and *unc-57(e406), unc-64 (e246)* double mutant animals. ***, $p < 0.001$.

Figure 5. Serine to Lysine mutations improved the function of KES1_rEndoA1 chimera *in vivo*.

(A) A helical wheel presentation of the KES1 ALPS motif. Arrows indicated the serine residues (S2, S3, and S4) that occupy the 1st turn of the helix, and S20 that resides on the opposite side to S4. The full sequence of the KES1 ALPS motif was listed below the helical wheel. **(B)** Representative locomotion

trajectories of transgenic *endophilin unc-57* mutant worms carrying KES1_rEndoA1 chimeras. The scale bar indicates 1 mm. **(C)** Quantification of locomotion rates. **(D)** Representative eEPSC traces and summary data for eEPSC amplitudes. ***, $p < 0.001$; when compared to *endophilin unc-57 mutants*. ###, $p < 0.001$; and #, $p < 0.05$; when compared to animals rescued by S4K,S20K mutant KES1_rEndoA1. **(E)** VGLUT-pHluorin responses from worms of indicated genotypes - *(left)* Mean fluorescence responses in ASH neurons, wild type (grey) and S4K,S20K KES1_rEndoA1 (purple), *(middle)* rate constants of fluorescence decay; and *(right)* basal levels of VGLUT-pHluorin fluorescence. Grey rectangle indicated "stimulation-on". Shading indicated SEM. **(F)** A representative transmission electron micrograph of synapses rescued by the S4K,S20K KES1_rEndoA1. **(G)** The abundance of SVs per synaptic profile was shown as mean ± standard error. The number of synaptic profiles analyzed for each genotype was indicated in the bar graphs. **(H)** The number of endosome-like (EL) structures per synapse. The number of synapses analyzed for each genotype was indicated in the bar graphs. ***, $p < 0.001$; **, $p < 0.01$; n.s., not significant.

Figure 6. Increases of positive net charges of the amphipathic helix improved the function of DivIVA_rEndoA1 chimeras.

(A). A helical wheel presentation of an ALPS motif of the bacteria protein DivIVA. Two glutamic acid residues (E4, E14) and an aspartic acid residue (D12) were changed to serine residues to generate the E4S,D12S,E14S version of DivIVA_rEndoA1. **(B)** Locomotion, **(C)** endogenous EPSCs, and **(D)** evoked EPSCs. **(E)** ASH VGLUT-pHluorin fluorescence**.** The results were plotted as described in the legends of Figures 3. The number of synapses analyzed for each genotype was indicated in the bar graphs. **(F)** Representative transmission electron micrographs of synapses rescued by DivIVA_rEndoA1 and the mutant E4S,D12S,E14S DivIVA_rEndoA1. Yellow shading indicated dense projections (DP). The white arrowheads show endosome-like structures. **(G)** The abundance of SVs per synaptic profile. The number of synaptic profiles analyzed for each genotype was indicated in the bar graphs. **(H)** The number of endosome-like (EL) structures per synapse was presented as mean ± standard error. The number of synapses analyzed for each genotype was indicated in the bar graphs. ***, $p < 0.001$. All data were shown as mean ± SEM.

Figure 7. Lysine-to-serine mutations disrupted the function of endophilin and induced accumulation of endosome-like structures at synapses.

(A) Lysine residues were highlighted in the sequence (top) and the helical wheel presentation (middle) of the H0 motif of rEndoA1. The net charge (+4) of rEndoA1 H0 was indicated (bottom) for clarity. Single-copy transgenes that encode GFP-tagged rEndoA1 were introduced into *unc-57* mutant worms. Four versions of lysine-to-serine (K-to-S) mutant rEndoA1 (including the single K16S, the double K7S,K16S, the triple K7S,K16S,K20S, and the quadruple K7S,K8S,K16S,K20S mutants) were examined for their ability to restore locomotion **(B)**, endogenous EPSCs **(C)**, and evoked EPSCs **(D)**. Representative transmission electron micrograph of synapses rescued by the K7S,K8S,K16S,K20S quadruple mutant rEndoA1 was shown in **(E)**. **(F)** The abundance of SVs per synaptic profile was shown as mean ± standard error. The number of synaptic profiles analyzed for each genotype was indicated in the bar graphs. **, $p < 0.01$; *n.s.*, not significant; compared to the quadruple K7S,K8S,K16S,K20S mutants. **(G)** The number of ELs per synapse was presented as mean ± standard error (*left*). ***, $p < 0.001$. The fraction of synapses with and without endosome-like structures was plotted for each genotype (*right*). The number of synapses analyzed for each genotype was indicated in the bar graphs.

Figure S1. GFP-tagged rEndoA1 chimeras were expressed in neurons at similar levels. Related to Figure 2.

(A) Single-copy transgenes were generated to express GFP-tagged rEndoA1 chimeras in C. elegans neurons. Expression levels of rEndoA1 chimeras in neurons were estimated by measuring background-subtracted fluorescence around nerve rings (a tight axon bundle made of processes from sensory and interneurons) in C. elegans. White arrowheads indicated nerve rings. Fluorescence intensity of rEndoA1 chimeras was normalized to that of wild type rEndoA1. Results were plotted in the bar graph. Error bars indicate SEM. **(B)** rEndoA1 chimeras were tagged at the C terminus with the red fluorescent protein mScarlet. The distribution of rEndoA1 chimera red fluorescence in DA neuron dorsal axons was compared with a co-expressed SV marker (GFP::Rab-3). Scale bars indicate 2μm. **(C)** Bafilomycin A1 (5 μM) treatment for 1 hour significantly increased the basal fluorescence intensity of VGLUT-pHluorin in wild type and KES1_rEndoA1 worms, but not in endophilin unc-57 mutant animals. ***, $p < 0.001$; n.s.,

not significant, when compared to untreated animals. Unpaired t-test. **(D-E)** Representative transmission electron micrographs of synapses form the following worms: unc-57 mutants carrying ΔH0_rEndoA1 **(D)**, and unc-57, unc-64 double mutants carrying KES1_rEndoA1 **(E)**.

Figure S2. Amphipathic helixes from endophilin, KES1, and NUP133 display distinct net charge properties. Related to Figure 2-4.

(A) Helical wheel presentations (top) and sequences (bottom) of amphipathic helices in KES1, NUP133, and rEndoA1. ALPS: amphipathic lipid packing sensor motif. Net electric charges of these amphipathic helices were shown (middle). Amino acid residues in the helical wheel presentations are colored as described in the legend of Figure 1. **(B)** The consensus sequences and the logo plots of conservation were shown in the left panels, for the amphipathic helices of KES1, NUP133, and endophilin. Amino acid residues in the logo plots were colored as follows: yellow - nonpolar; green - polar; blue - basic; red - acidic. The net charge histograms of the amphipathic helices were shown in the right panels. Logo plots were generated using Geneious Prime 2021.1. Net charge was calculated for each helix using established amino acid properties at physiological pH.

Figure S3. The membrane tubulation activity of wild type and chimeric versions endophilin are regulated by the abundance of anionic phospholipids. Related to Figure 5.

(A) Transmission electron micrographs for liposomes (2 mM total lipids) incubated with wild type rEndoA1 (4 μM) for 5 min at room temperature. Liposomes were prepared by extrusion through filters with 0.2 μm pore size. The lipid compositions of liposomes were 15%PS/85%PC (left), 25%PS/0.5%PIP2/74.5%PC (middle), and 25%PS/2%PIP2/73%PC (right). **(B)** Quantification of membrane tubulation. (left) Tubulation Fraction = (# of liposomes with extended protrusions) / (# of total liposomes). (right) The length of membrane tubules was determined using ImageJ. Error bars indicate SEM. ***, $p < 0.001$. One-way ANOVA followed by Dunnett's test was used for statistical analysis. **(C)** Transmission electron micrographs for liposomes incubated with wild type and chimeric rEndoA1 proteins; (left) wild type rEndoA1, (middle) KES1_rEndoA1, and (right) NUP133_rEndoA1. Liposomes were prepared by extrusion through filters with 0.2 μm pore size. The lipid composition of these liposomes was 25%PS/0.5%PIP2/74.5%PC. Wild type and chimeric rEndoA1 proteins (4μM) were incubated with

liposomes (2 mM total lipids) for 5 min at the room temperature. Reaction was stopped by fixing with 0.5x Karnovsky's solution. Scale bars: 200 nm. **(D)** Quantification of membrane tubulation. Tubulation Fraction = (# of liposomes with extended protrusions) / (# of total liposomes). Liposomes contained either 15%PS/85%PC, 25%PS/0.5%PIP2/74.5%PC, or 25%PS/2%PIP2/73%PC, respectively. Error bars indicate SEM. ***, $p < 0.001$, compared to liposomes incubated with wild type rEndoA1. One-way ANOVA followed by Dunnett's test was used for statistical analysis.

Figure S4. S/K mutations improved the ability of KES1_rEndoA1 chimera to support endogenous synaptic activity in vivo. Related to Figure 5.

(A) Representative traces of endogenous excitatory postsynaptic currents that were recorded at neuromuscular junctions were shown for indicated genotypes. Single-copy transgenes were introduced to drive pan-neuronal expression of KES1_rEndoA1 variants in endophilin unc-57(e406) mutant worms. **(B)** Summary data for endogenous EPSC rates (left) and amplitudes (right) were shown. ***, $p < 0.001$; when compared to endophilin unc-57 mutants. ###, $p < 0.001$; and #, $p < 0.05$; when compared to animals rescued by S4K,S20K mutant KES1_rEndoA1. The number of worms analyzed for each genotype is indicated in the bar graphs. Error bars indicate SEM. One-way ANOVA followed by Dunnett's test was used for statistical analysis.

Figure S5. The impact of K/S mutations in the rEndoA1 H0 helix on locomotory and electrophysiological features. Related to Figure 7.

(A) Quantification of locomotion rates. Mutant rEndoA1 chimeras with single Lys-to-Ser and Glu-to-Ser mutations were examined for their ability to restore locomotion activity in endophilin unc-57 mutant worms. The number of worms analyzed for each genotype is shown in the bar graphs. Error bars represent SEM. **(B)** The amplitude of endogenous EPSCs was plotted for Lys-to-Ser mutants of rEndoA1. Error bars represent SEM. The number of worms analyzed for each genotype is indicated in the bar graphs.

Figure S6. The electrostatic property of the HI helix is important for endophilin's function. Related to Figure 7.

(left) The sequence (top) and the helical wheel presentations (bottom) of the amphipathic HI helix of rEndoA1. ***(right)*** Quantification of locomotion rates. Mutant rEndoA1 chimeras with Lys-to-Ser mutations were examined for their ability to restore locomotion activity in endophilin unc-57 mutant worms. The number of worms analyzed for each genotype is shown in the bar graphs. Error bars represent SEM.

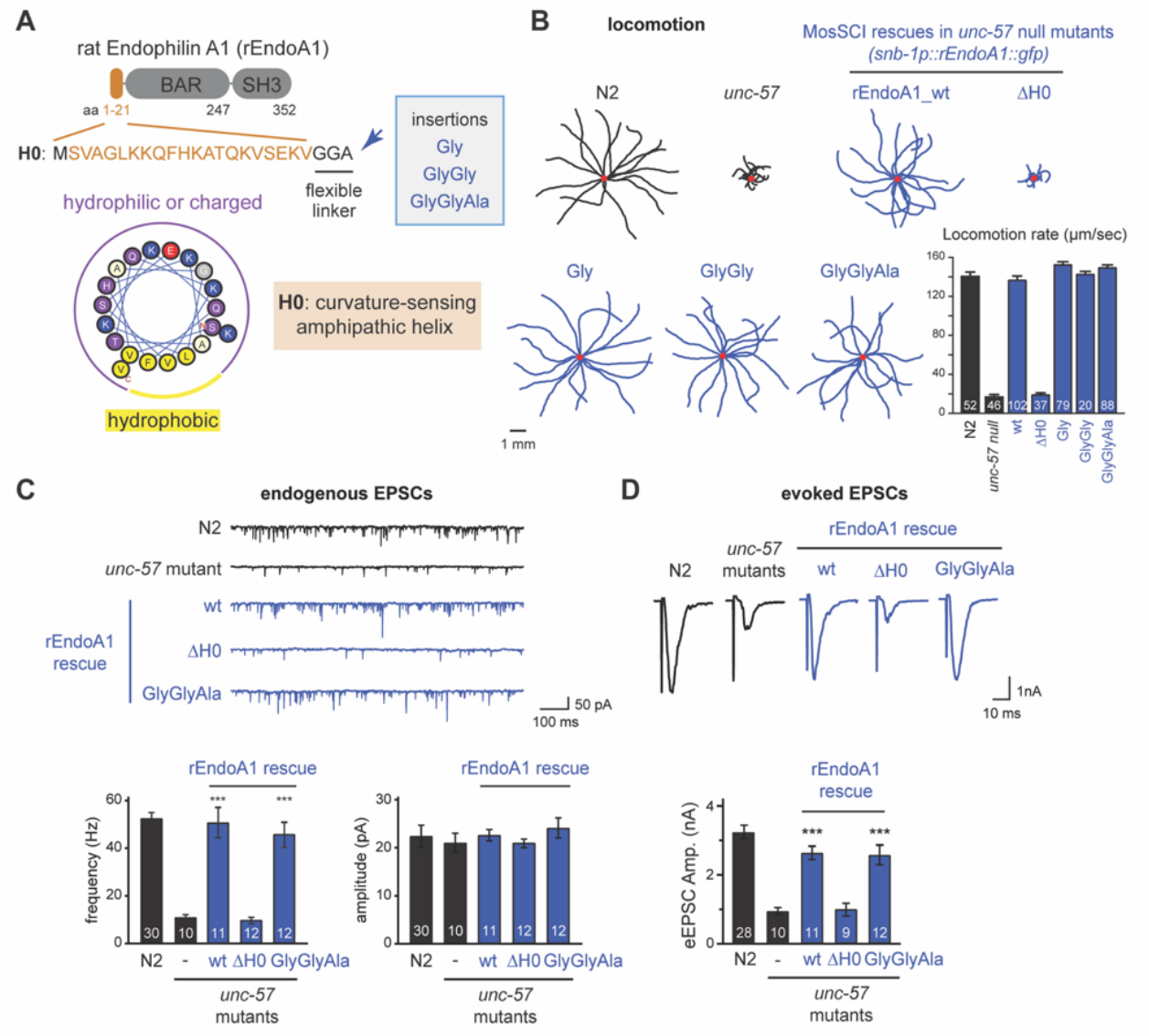
A
rat Endophilin A1 (rEndoA1)
BAR
SH3
aa 1-21
247
352
H0: MSVAGLKKQFHKATQKVSEKVGGA
flexible linker
insertions
Gly
GlyGly
GlyGlyAla
hydrophilic or charged
hydrophobic
H0: curvature-sensing amphipathic helix
B
locomotion
MosSCI rescues in unc-57 null mutants
(snb-1p::rEndoA1::gfp)
N2
unc-57
rEndoA1_wt
ΔH0
Gly
GlyGly
GlyGlyAla
1 mm
Locomotion rate (μm/sec)
160
120
80
40
0
52
46
102
37
79
20
88
N2
unc-57 null
wt
ΔH0
Gly
GlyGly
GlyGlyAla
C
endogenous EPSCs
N2
unc-57 mutant
wt
ΔH0
GlyGlyAla
rEndoA1 rescue
50 pA
100 ms
rEndoA1 rescue
frequency (Hz)
60
40
20
0
***
***
30
10
11
12
12
N2
-
wt
ΔH0
GlyGlyAla
unc-57 mutants
rEndoA1 rescue
amplitude (pA)
30
20
10
0
30
10
11
12
12
N2
-
wt
ΔH0
GlyGlyAla
unc-57 mutants
D
evoked EPSCs
rEndoA1 rescue
N2
unc-57 mutants
wt
ΔH0
GlyGlyAla
1nA
10 ms
rEndoA1 rescue
eEPSC Amp. (nA)
4
2
0
***
***
28
10
11
9
12
N2
-
wt
ΔH0
GlyGlyAla
unc-57 mutants

Figure 1. 1

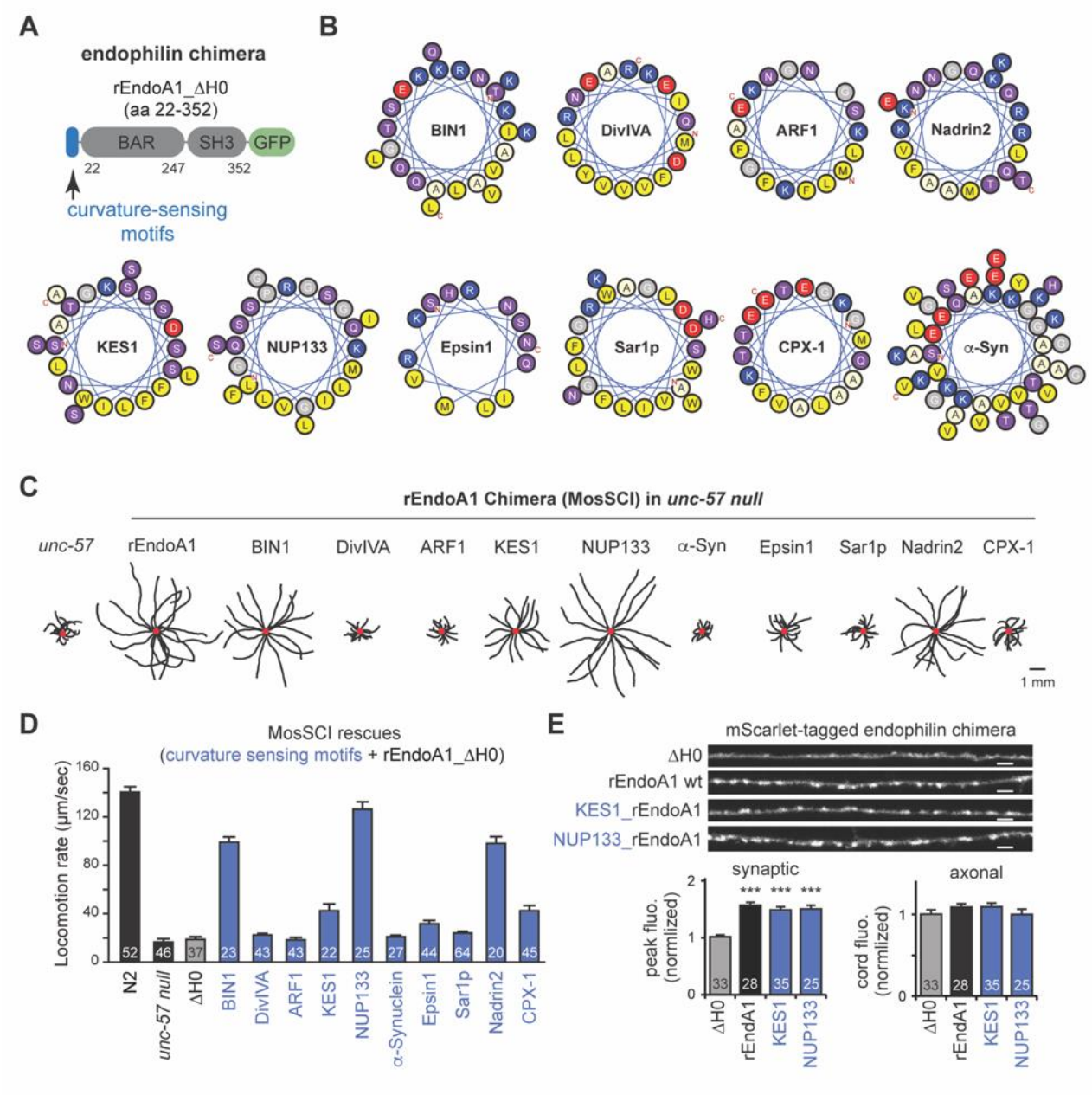
A
endophilin chimera
rEndoA1_ΔH0
(aa 22-352)
BAR
SH3
GFP
22
247
352
curvature-sensing
motifs
B
BIN1
DivIVA
ARF1
Nadrin2
KES1
NUP133
Epsin1
Sar1p
CPX-1
α-Syn
C
rEndoA1 Chimera (MosSCI) in unc-57 null
unc-57
rEndoA1
BIN1
DivIVA
ARF1
KES1
NUP133
α-Syn
Epsin1
Sar1p
Nadrin2
CPX-1
1 mm
D
MosSCI rescues
(curvature sensing motifs + rEndoA1_ΔH0)
Locomotion rate (µm/sec)
160
120
80
40
0
52
46
37
23
43
43
22
25
27
44
64
20
45
N2
unc-57 null
ΔH0
BIN1
DivIVA
ARF1
KES1
NUP133
α-Synuclein
Epsin1
Sar1p
Nadrin2
CPX-1
E
mScarlet-tagged endophilin chimera
ΔH0
rEndoA1 wt
KES1_rEndoA1
NUP133_rEndoA1
synaptic
axonal
peak fluo.
(normlized)
cord fluo.
(normlized)
***
***
***
2
1
0
33
28
35
25
ΔH0
rEndA1
KES1
NUP133

Figure 1. 2

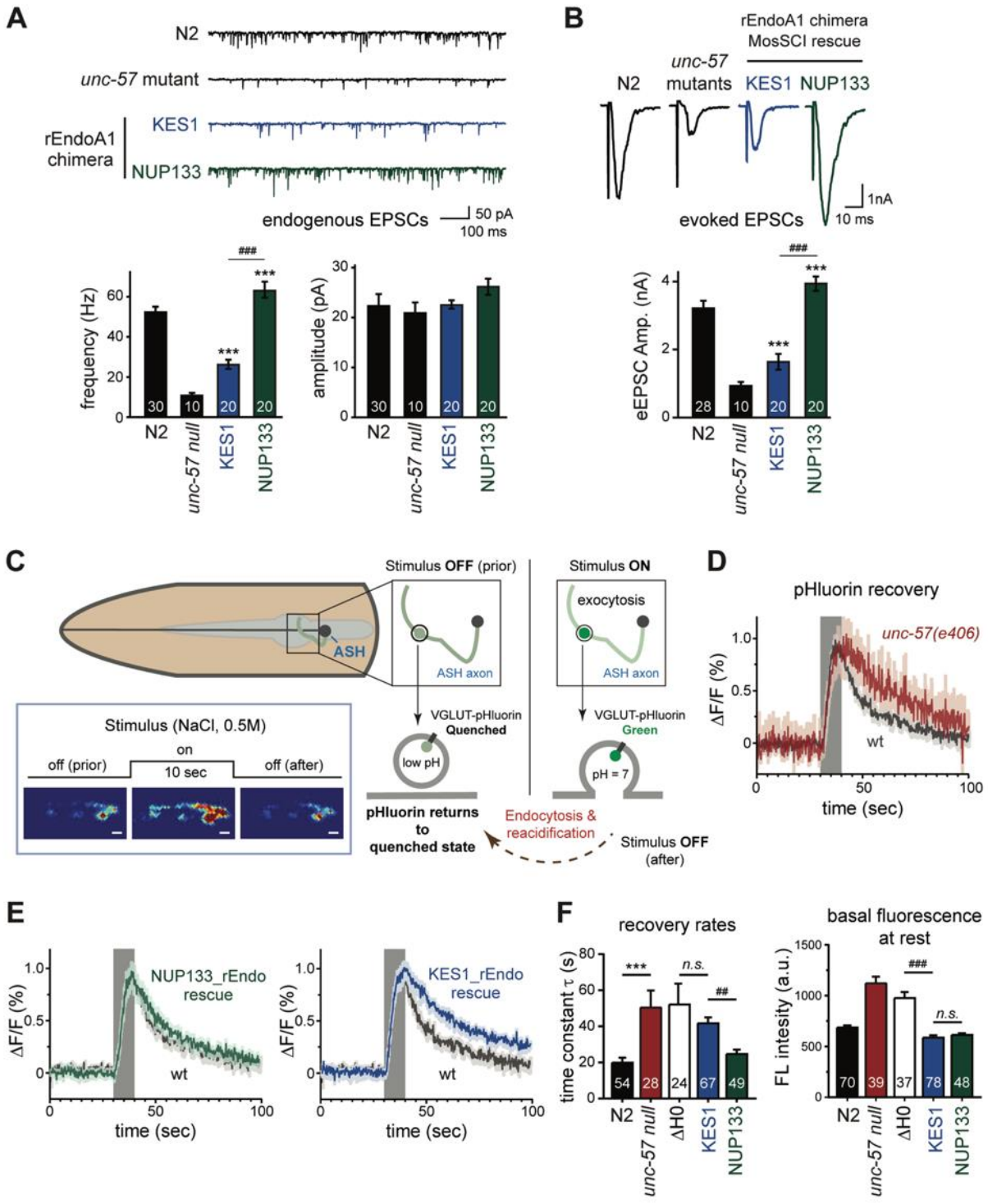
A
N2
unc-57 mutant
rEndoA1 chimera
KES1
NUP133
endogenous EPSCs
50 pA
100 ms
frequency (Hz)
amplitude (pA)
N2
unc-57 null
KES1
NUP133
B
rEndoA1 chimera
MosSCI rescue
unc-57 mutants
evoked EPSCs
1nA
10 ms
eEPSC Amp. (nA)
C
Stimulus OFF (prior)
Stimulus ON
ASH
ASH axon
exocytosis
VGLUT-pHluorin Quenched
VGLUT-pHluorin Green
low pH
pH = 7
Stimulus (NaCl, 0.5M)
off (prior)
on
10 sec
off (after)
pHluorin returns to quenched state
Endocytosis & reacidification
Stimulus OFF (after)
D
pHluorin recovery
unc-57(e406)
wt
ΔF/F (%)
time (sec)
E
NUP133_rEndo rescue
KES1_rEndo rescue
wt
ΔF/F (%)
time (sec)
F
recovery rates
time constant τ (s)
n.s.
basal fluorescence at rest
FL intesity (a.u.)
N2
unc-57 null
ΔH0
KES1
NUP133

Figure 1. 3

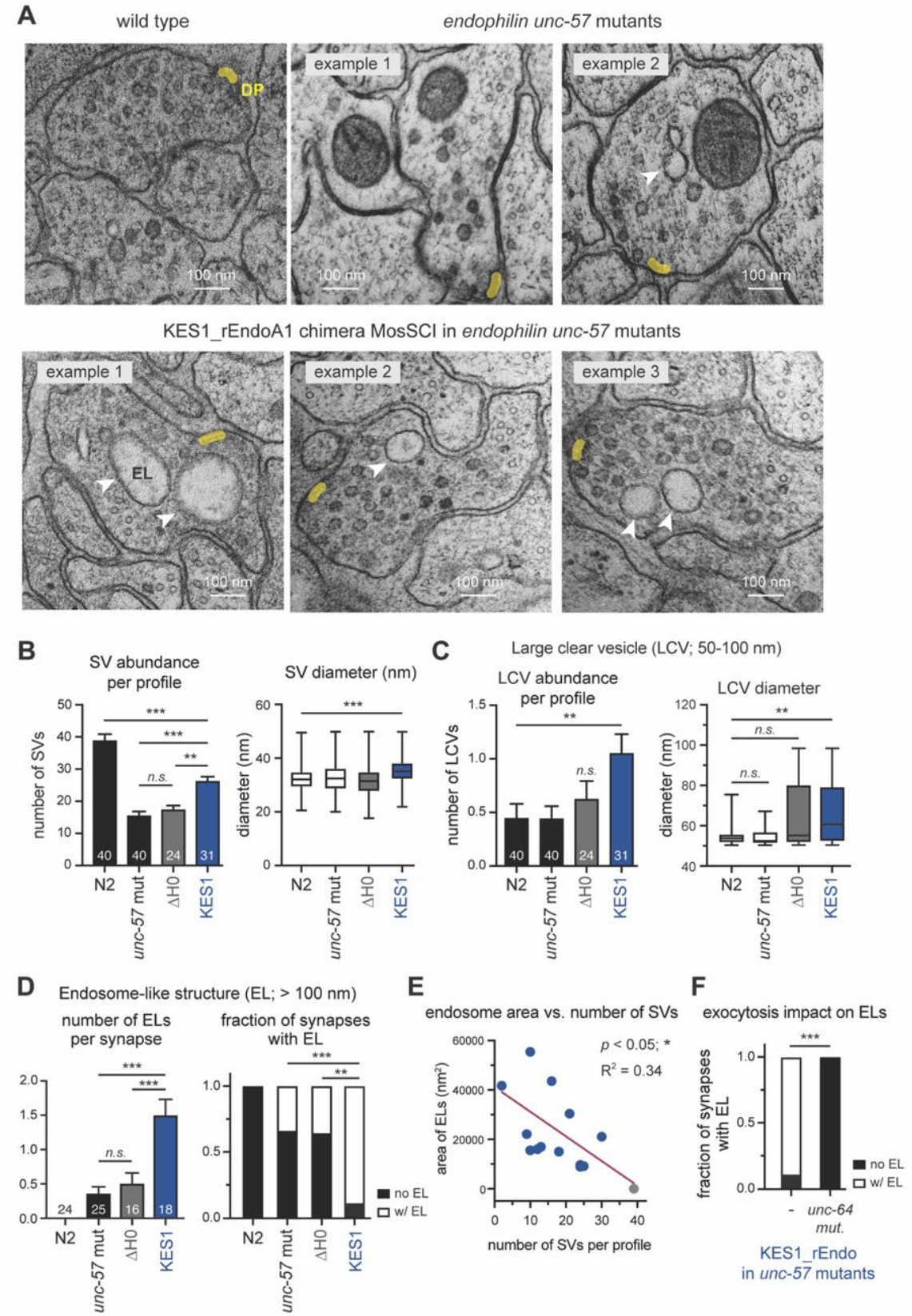
A
wild type
endophilin unc-57 mutants
DP
example 1
example 2
100 nm
KES1_rEndoA1 chimera MosSCI in endophilin unc-57 mutants
example 3
EL
B
SV abundance per profile
number of SVs
SV diameter (nm)
diameter (nm)
N2
unc-57 mut
ΔH0
KES1
C
Large clear vesicle (LCV; 50-100 nm)
LCV abundance per profile
number of LCVs
LCV diameter
n.s.
D
Endosome-like structure (EL; > 100 nm)
number of ELs per synapse
fraction of synapses with EL
no EL
w/ EL
E
endosome area vs. number of SVs
p < 0.05; *
R2 = 0.34
area of ELs (nm2)
number of SVs per profile
F
exocytosis impact on ELs
unc-64 mut.
KES1_rEndo in unc-57 mutants

Figure 1. 4

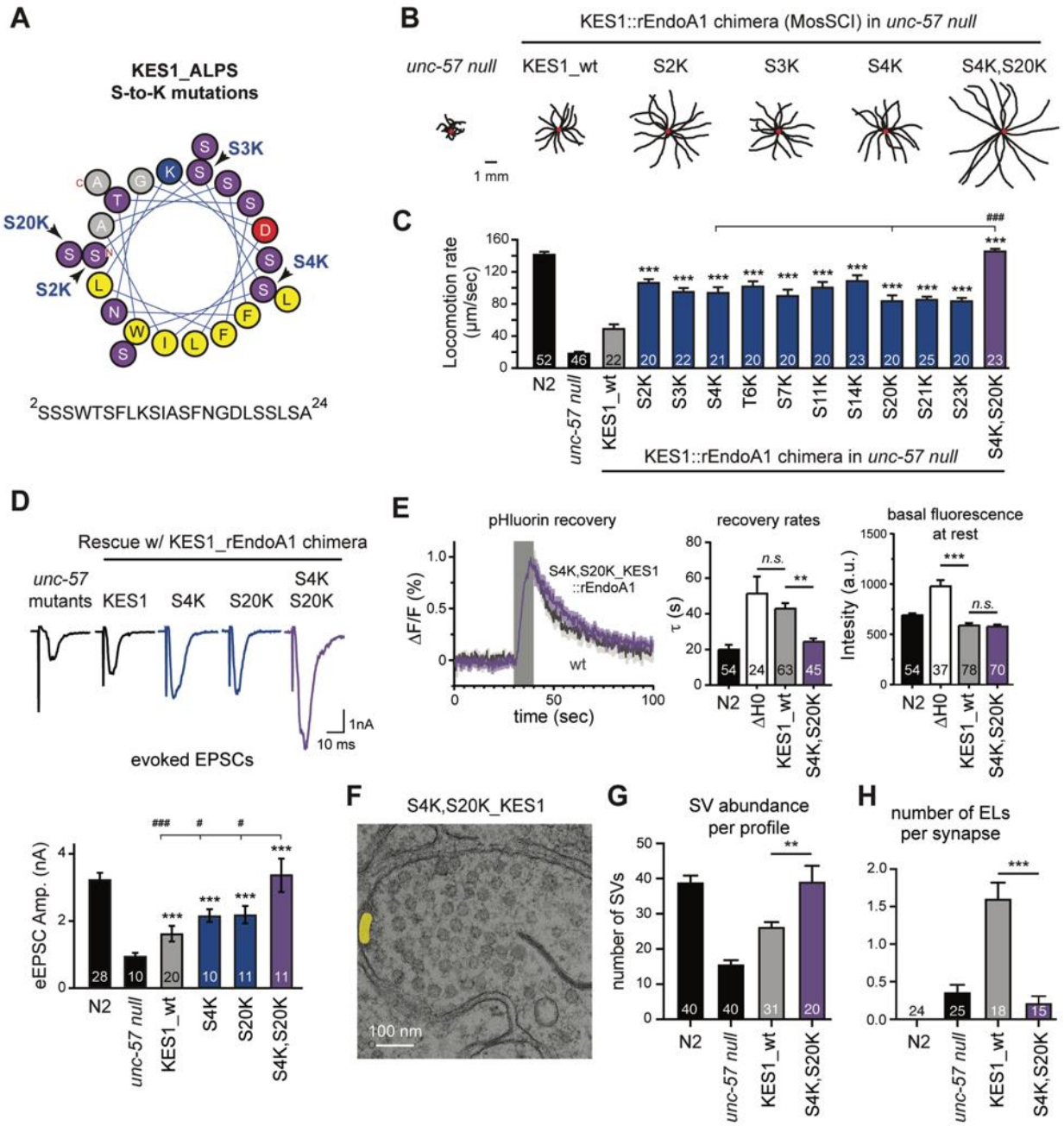
A
KES1_ALPS
S-to-K mutations
S3K
S20K
S4K
S2K
2SSSWTSFLKSIASFNGDLSSLSA24
B
KES1::rEndoA1 chimera (MosSCI) in unc-57 null
unc-57 null
KES1_wt
S2K
S3K
S4K
S4K,S20K
1 mm
C
Locomotion rate (µm/sec)
N2
unc-57 null
KES1_wt
S2K
S3K
S4K
T6K
S7K
S11K
S14K
S20K
S21K
S23K
S4K,S20K
KES1::rEndoA1 chimera in unc-57 null
D
Rescue w/ KES1_rEndoA1 chimera
unc-57 mutants
KES1
S4K
S20K
S4K S20K
1nA
10 ms
evoked EPSCs
eEPSC Amp. (nA)
E
pHluorin recovery
S4K,S20K_KES1 ::rEndoA1
wt
ΔF/F (%)
time (sec)
recovery rates
τ (s)
ΔH0
basal fluorescence at rest
Intesity (a.u.)
n.s.
F
S4K,S20K_KES1
100 nm
G
SV abundance per profile
number of SVs
H
number of ELs per synapse

Figure 1. 5

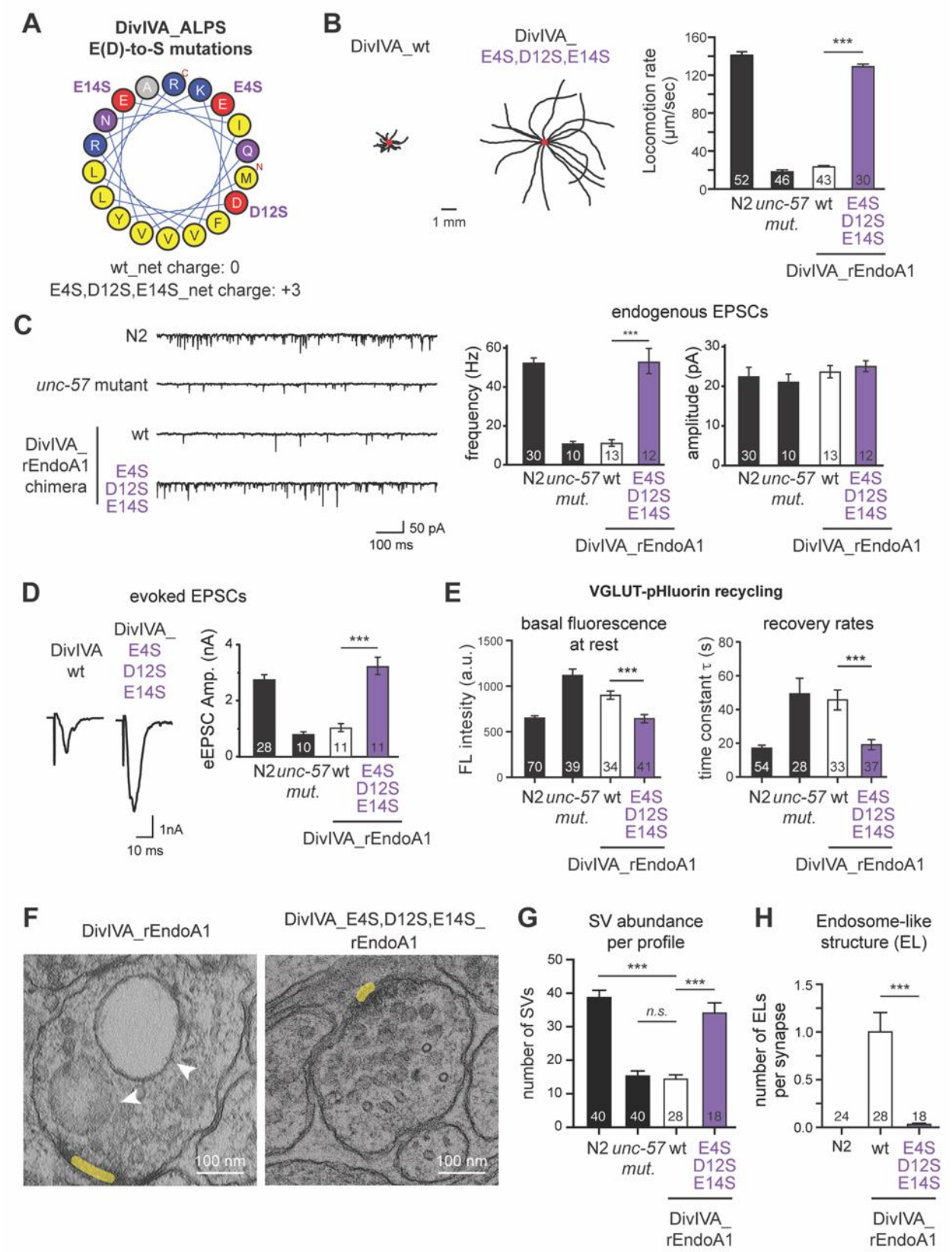
A
DivIVA_ALPS
E(D)-to-S mutations
E14S
E4S
D12S
wt_net charge: 0
E4S,D12S,E14S_net charge: +3
B
DivIVA_wt
DivIVA_
E4S,D12S,E14S
1 mm
Locomotion rate (μm/sec)
N2
unc-57 mut.
wt
E4S D12S E14S
DivIVA_rEndoA1
C
N2
unc-57 mutant
DivIVA_ rEndoA1 chimera
wt
E4S D12S E14S
50 pA
100 ms
endogenous EPSCs
frequency (Hz)
amplitude (pA)
D
evoked EPSCs
DivIVA wt
DivIVA_ E4S D12S E14S
eEPSC Amp. (nA)
1nA
10 ms
E
VGLUT-pHluorin recycling
basal fluorescence at rest
FL intesity (a.u.)
recovery rates
time constant τ (s)
F
DivIVA_rEndoA1
DivIVA_E4S,D12S,E14S_ rEndoA1
100 nm
G
SV abundance per profile
number of SVs
n.s.
H
Endosome-like structure (EL)
number of ELs per synapse

Figure 1. 6

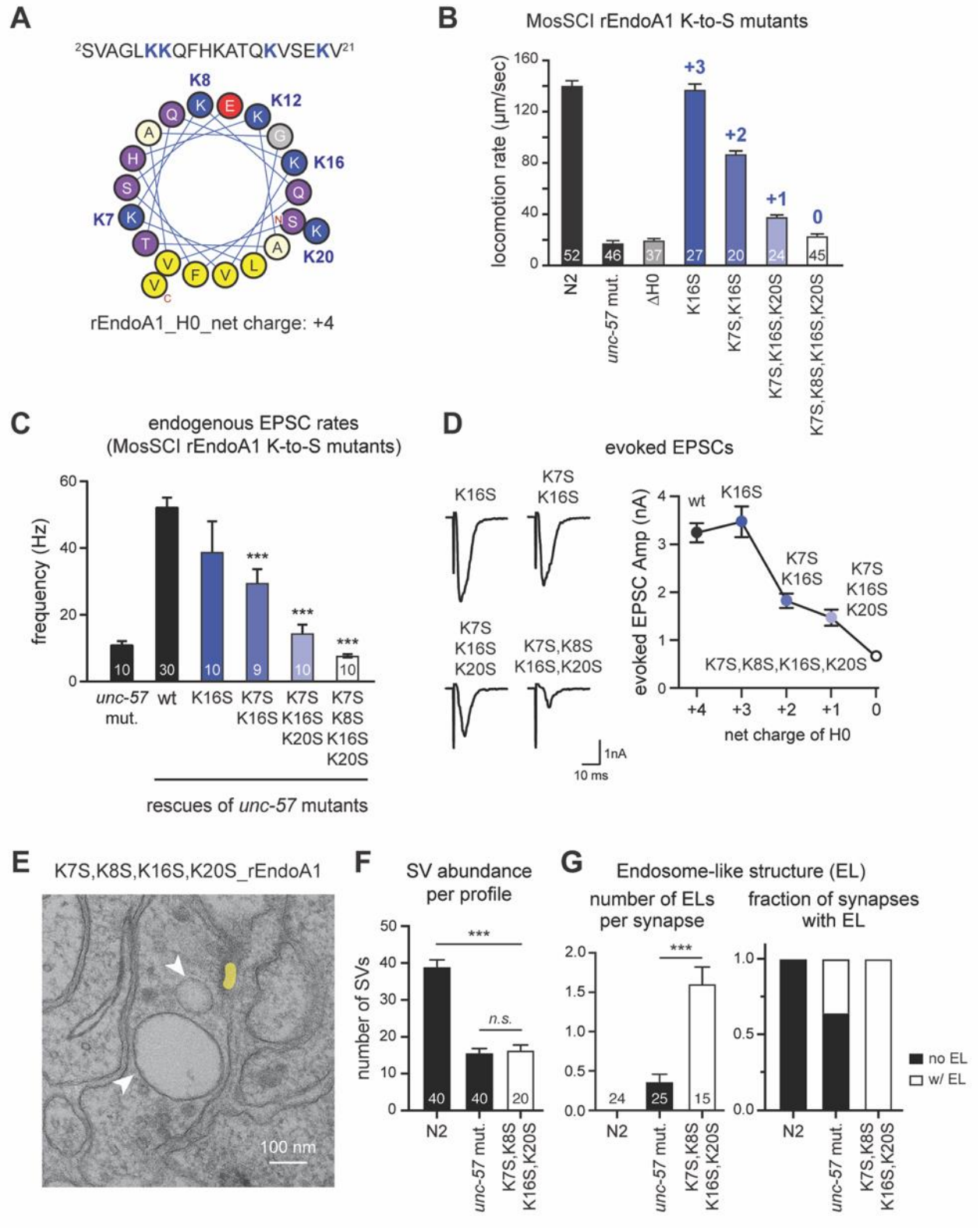
A
²SVAGLKKQFHKATQKVSEKV²¹
K8
K12
K16
K7
K20
rEndoA1_H0_net charge: +4
B
MosSCI rEndoA1 K-to-S mutants
locomotion rate (µm/sec)
+3
+2
+1
0
N2
unc-57 mut.
ΔH0
K16S
K7S,K16S
K7S,K16S,K20S
K7S,K8S,K16S,K20S
C
endogenous EPSC rates
(MosSCI rEndoA1 K-to-S mutants)
frequency (Hz)
unc-57 mut.
wt
K16S
K7S K16S
K7S K16S K20S
K7S K8S K16S K20S
rescues of unc-57 mutants
D
evoked EPSCs
K16S
K7S K16S
K7S K16S K20S
K7S,K8S K16S,K20S
1nA
10 ms
evoked EPSC Amp (nA)
net charge of H0
K7S,K8S,K16S,K20S
E
K7S,K8S,K16S,K20S_rEndoA1
100 nm
F
SV abundance per profile
number of SVs
n.s.
G
Endosome-like structure (EL)
number of ELs per synapse
fraction of synapses with EL
no EL
w/ EL

Figure 1. 7

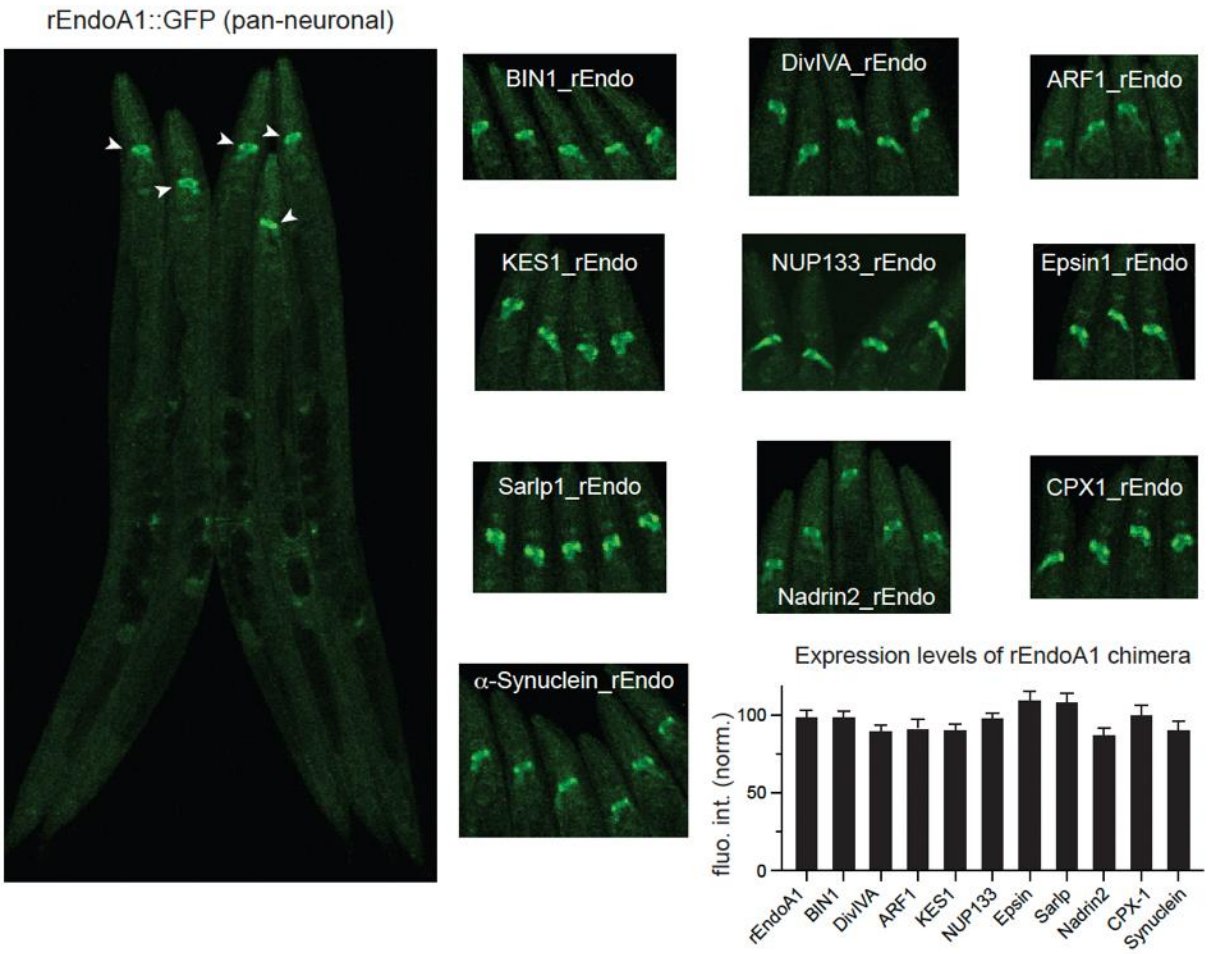

Suppl. figure 1

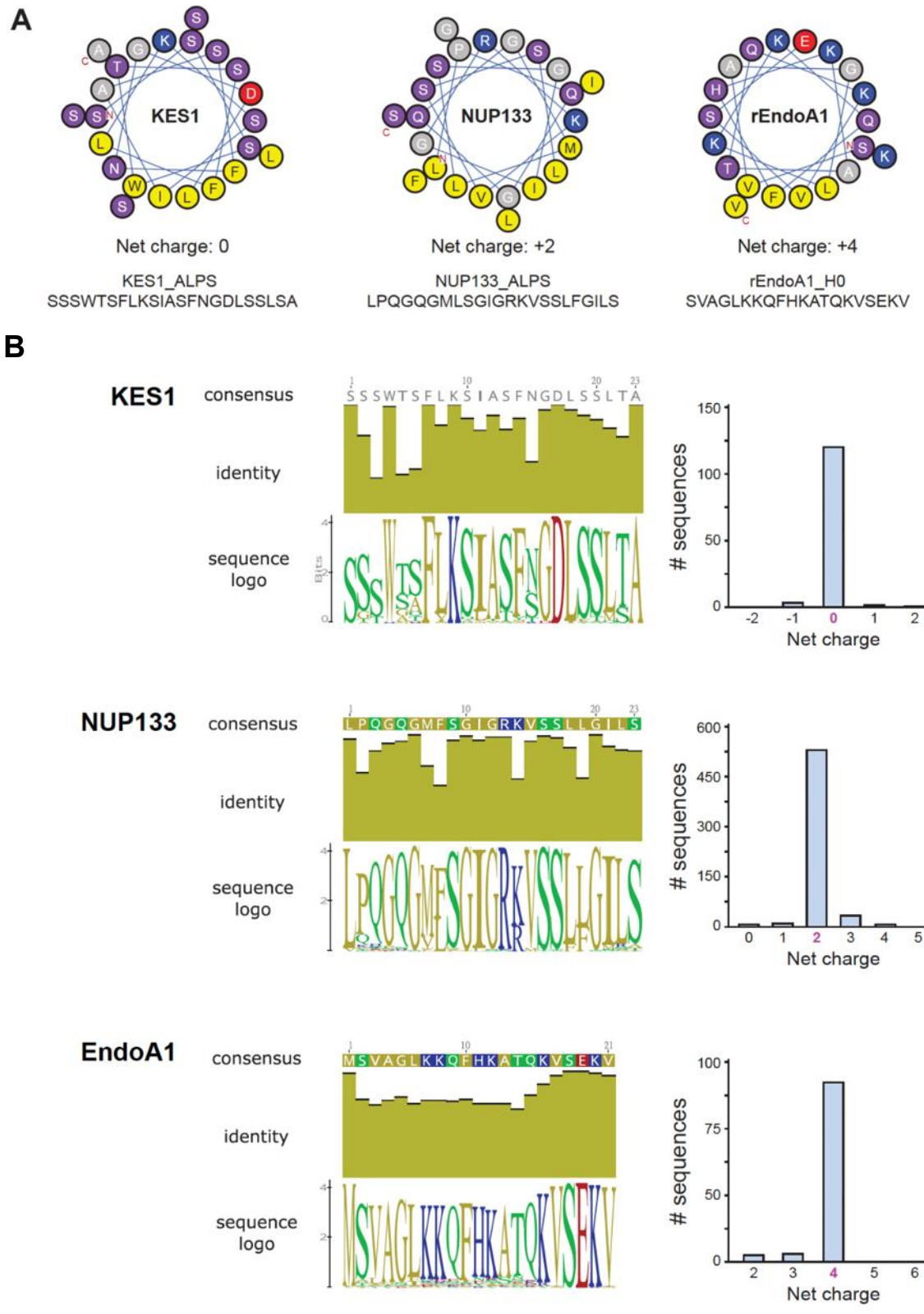

Suppl. figure 2

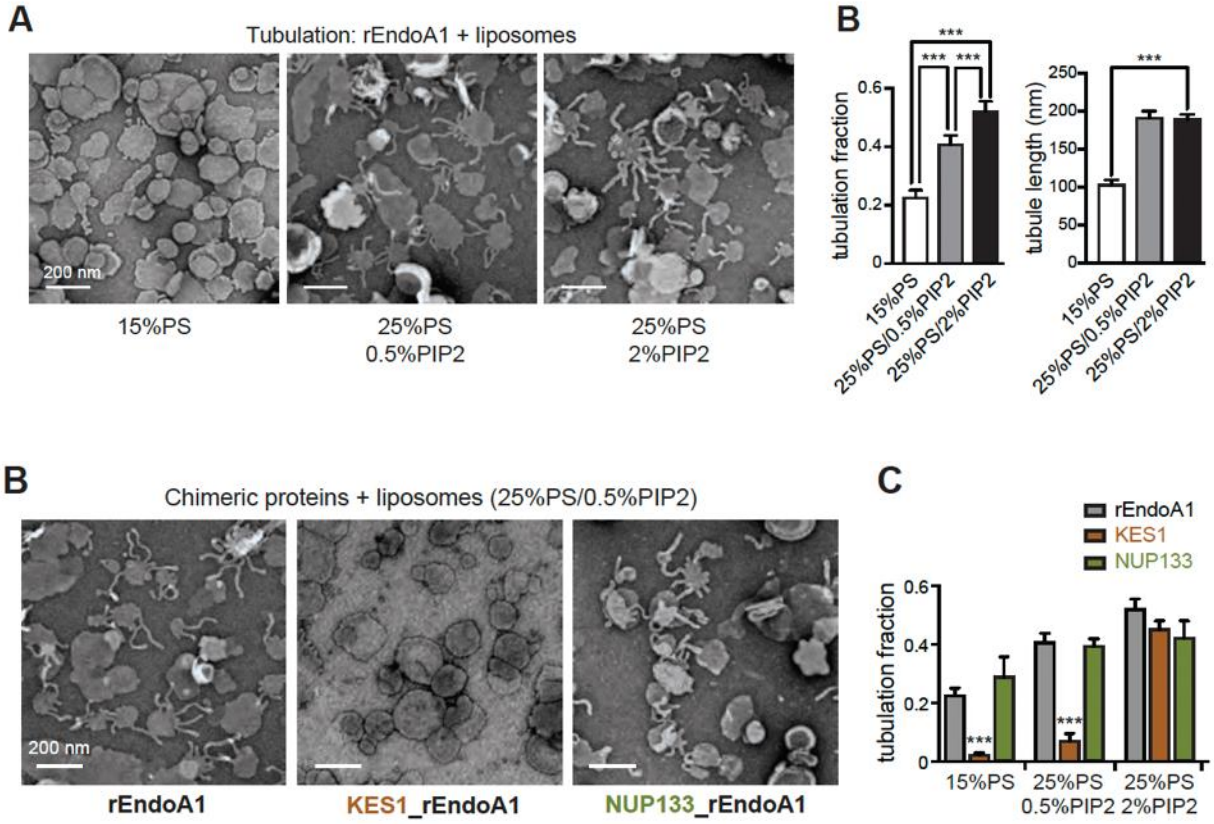

Suppl. figure 3

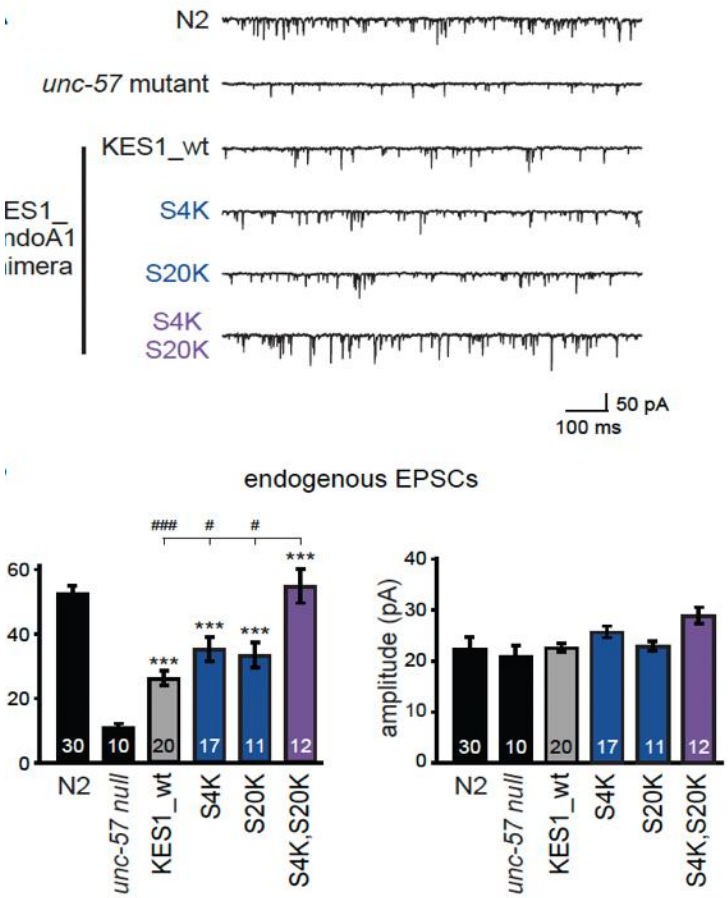

Suppl. figure 4

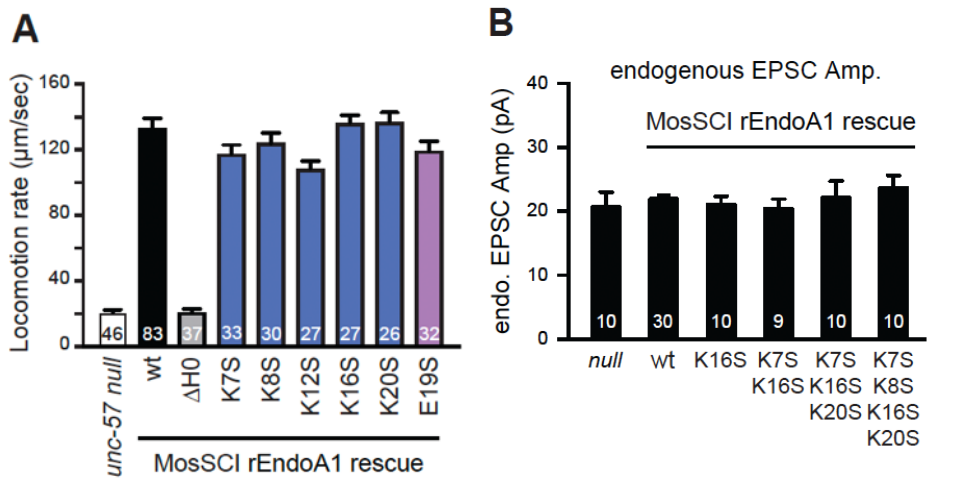

Suppl. figure 5

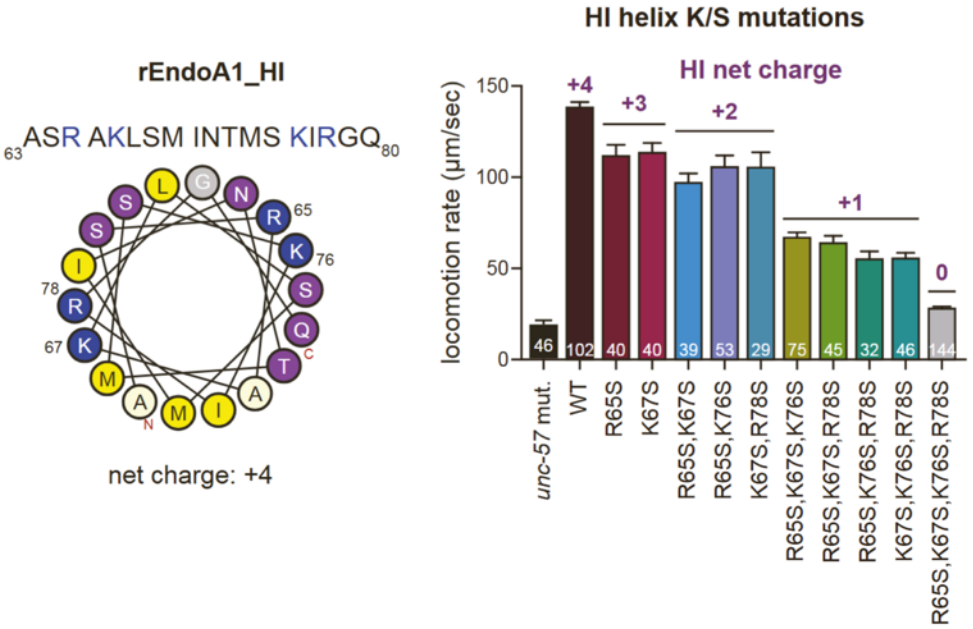

Suppl. figure 6

2.7 STAR Methods

LEAD CONTACT AND MATERIALS AVAILABILITY

Further information and requests for resources and reagents should be directed to, and will be fulfilled by, the Lead Contact, Jihong Bai (jbai@fredhutch.org).

MATERIALS AVAILABILITY

Plasmids and transgenic *C. elegans* lines generated in this study will be made available on request to the lead contact. This study did not generate new unique reagents.

DATA AND CODE AVAILABILITY

- All data reported in this paper will be shared by the lead contact upon request.
- This paper does not report original code.
- Any additional information required to reanalyze the data reported in this paper is available from the lead contact upon request.

KEY RESOURCES TABLE

REAGENT OR RESOURCE	SOURCE	IDENTIFIER
Bacterial		
E. coli: OP50	CGC	OP50
Chemicals and Critical Commercial Assays		
PrimeSTAR GXL DNA Polymerase	TaKaRa	Cat # R050A
PrimeSTAR Max DNA Polymerase	TaKaRa	Cat # R045B

Phusion polymerase	NEB Biolabs	Cat # M0530S
Gateway BP Clonase II	ThermoFisher	Cat # 11789100
Gateway LR Clonase II	ThermoFisher	Cat # 11791020
Ni-NTA agarose beads	Qiagen	Cat. # 157030990
HEPES	ThermoFisher	Cat. # BP310-500
Isopropyl–d-thiogalactopyranoside (IPTG)	ThermoFisher	Cat. # BP1620-10
Dithiothreitol	Boston BioProducts	Cat. # P765
2,3-butanedione monoxime (BDM)	Sigma	Cat. # B0753
Agar	Apex	Cat. # 20-275
QIAquick PCR Purification Kit	QIAGEN	Cat # 28104
Bafilomycin A1	Research Products International Corp.	Cat # B40500
Dimethyl sulfoxide (DMSO)	Sigma	Cat. # D8418
Experimental Models: Organisms/Strains	Supplemental Table 1	
Recombinant DNA	Supplemental Table 2	
Software and imagining equipment		

Excel	Microsoft	https://www.microsoft.com/en-us/microsoft-365/excel
Prism 9	GraphPad Prism	https://www.graphpad.com/scientific-software/prism/
WormLab Imaging System	MBF Bioscience, VT, USA	https://www.mbfbioscience.com/wormlab
Olympus FV-1000 Confocal Microscope	Olympus Company	https://www.olympus-lifescience.com/en/technology/museum/micro/2004/
SnapGene 5.0	SnapGene	https://www.snapgene.com
Igor Pro	Wavemetrics, OR, USA	https://www.wavemetrics.com
MATLAB	MathWorks, Inc., Natick, MA	https://www.mathworks.com/products/matlab.html

Note: rEndoA1 indicates rat endophilin A1

EXPERIMENTAL MODEL AND SUBJECT DETAILS

Worm strains were maintained at 22°C on NGM (nematode growth medium) agar plates seeded with Escherichia coli OP50 bacteria according to standard protocols (Brenner 1974). Unless otherwise specified, all experiments were carried out using day 1 adult hermaphrodites. Mutant and transgenic alleles were backcrossed at least 4 times against N2 Bristol strains.

2.8 METHOD DETAILS

Molecular Biology

DNA plasmids were constructed using the Multisite Gateway system (Invitrogen, Waltham, MA, USA) and Gibson assembly protocols (Gibson et al., 2009). All constructs were sequence verified. cDNA encoding rat endophilinA1 (rEndoA1) was amplified as previously described (Bai et al., 2010). The promoters used in this study are *Psnb-1* (3kb, for rescue experiments) and *Punc-129* (2.6kb, for imaging analyses). These promoters were cloned into modified pCFJ150 and pCFJ356 vectors (Frokjaer-Jensen et al., 2008) along with the cDNA of gene of interest. To build chimeric endophilin variants, the H0 helix (residues 2-21, SVAGLKKQFHKATQKVSEKV) of rat endophilin A1 was replaced with known amphipathic helices (listed below). DNA constructs encoding chimeric endophilin variants were generated using overlap extension PCR strategy (Higuchi et al., 1988). To construct plasmids for recombinant protein expression, DNA fragments encoding genes of interest were inserted into a modified PET28A vector (Novagen, Madison, WA) containing a His6 tag to facilitate purification.

BIN1_AH [8-33, *H. sapiens*]

VTAGKIASNVQKKLTRAQEKVLQKL

5'-gtgactgctggaaaaatagcttcaaatgtccagaagaagttgactcgtgcccaagagaaggttctccaaaaactc-3'

ARF1_AH [1-17, *H. sapiens*]

MGNIFANLFKGLFGKKE

5'-atgggtaacatctttgccaacctgtttaaaggtctttttggcaagaaggag-3'

NUP133_AH [245-267, *H. sapiens*]

LPQGQGMLSGIGRKVSSLFGILS

5'-cttccacaaggtcagggcatgctcagtggaattggtagaaaagtatcttcattgttcggaatcctttca-3'

KES1_AH [7-29, *S. cerevisiae*]

SSSWTSFLKSIASFNGDLSSLSA

5’-tcatcatcctggacatctttcctgaaatctatcgcttcctttaatggtgatttgtcgtcgctgagtgcc-3’

Sar1p_AH [1-23]

MAGWDIFGWFRDVLASLGLWNKH

5’-*atggccggatgggacatcttcggatggttccgtgacgtccttgcctcccttggactttggaacaagcac*-3’

EPN1_AH [3-16, *H. sapiens*]

TSSLRRQMKNIVHN

5’-*acgtcttcccttcgaagacagatgaaaaacatagtacataac*-3’

CPX-1_AH [115-135, *C. elegans*]

LGLTEQVEKAKTMATGAFETV

5’-*ctcgggctcacggagcaagtcgaaaaagcgaaaactatggcgaccggcgccttcgagaccgtc*-3’

divIVA_AH [25-41, *B. subtilis*]

VNEFLAQVRKDYEIVLR

5’-*gtcaacgagttccttgcccaagtccgtaaggactacgagatcgtcctccgt*-3’

alpha-synuclein [9-52, *H. sapiens*]

SKAKEGVVAAAEKTKQGVAEAAGKTKEGVLYVGSKTKEGVVHGV

5’-tccaaggccaaggagggagtcgtcgccgctgctgagaagactaagcaaggagttgctgaggctgctggaaagactaaggaggg

agttctttacgttggatctaagaccaaggagggagtcgttcacggagtc-3’

Recombinant Protein Production

Recombinant proteins were expressed as N-terminal his6-SUMO-tagged fusion proteins in the BL21(DE3) *E. coli* strain. Protein purification and tag removal were carried out using published protocols (Poudel et al., 2016). Briefly, the bacteria culture was grown in Luria Broth medium at 37°C. When OD_{600} reached 1.0, isopropyl-D-thiogalactopyranoside was added to the bacterial culture (0.2mM) to induce

protein expression. The bacterial culture was further grown overnight at 15°C. Bacteria harvested by centrifugation was lysed by a microfluidizer in the lysis buffer (20 mM HEPES, pH 8.0, 300 mM NaCl, 15 mM imidazole). Proteins were purified using NiNTA-agarose beads (Qiagen, Valencia, CA), and then eluted with a lysis buffer plus 250 mM imidazole. Recombinant endophilinA1 variants were expressed as his6-SUMO-tagged fusion proteins. The SUMO protease ULP1 (ubiquitin-like-specific protease 1) was used to cleave off his6-SUMO tags, resulting in endophilin A1 variants with native N-terminal amino acid compositions. His6-SUMO fragments cleaved off by ULP1 were removed using NiNTA-agarose beads (Qiagen, Valencia, CA). Purified proteins were dialyzed against the HEPES buffer (50 mM HEPES, pH 7.4, 150mM NaCl) plus 1 mM DTT. Proteins were stored at 4°C.

Transgenes and Germline Transformation

Transgenic strains were generated by microinjection. Mos1-mediated single-copy transgene insertion methods were used to produce animals carrying single-copy transgenes (Frokjaer-Jensen et al., 2008, Frokjaer-Jensen et al., 2012). Mos1 target sites used in this study are *ttTi5605* (chromosome II) and *cxTi10816* (chromosome IV). Transgenic worms were outcrossed at least four times.

Worm Tracking and Locomotion Analysis

Young adult animals (day 1) were picked to 10 cm agar plates with no bacterial lawn (20 worms per plate). Imaging began 1 hour after worms were transferred. Worm crawling on the agar surface was recorded for 30 seconds using the WormLab Imaging System (MBF Bioscience, VT, USA). The center of mass was determined for each animal using custom object-tracking software developed using ImageJ (Schneider et al., 2012). Average speed was determined for each animal.

Confocal Microscopy and Analysis

Animals were immobilized with 2,3-Butanedione monoxamine (30 mg/ml; Sigma-Aldrich), and were mounted on 2% agarose pads for imaging. Fluorescence images were collected on an inverted Olympus IX81 microscope, using a laser scanning confocal imaging system (Olympus FluoView FV1000) and an Olympus UPLSAPO 60x 1.4 NA Oil immersion objective (at 5x zoom). GFP and mNeonGreen were

excited using a 488 nm Argon laser and mScarlet was excited using a 559 nm diode pumped solid state laser. Rat endophilinA1 (rEndoA1) variants used in the rescue experiments were C-terminally tagged with GFP. Expression levels of rEndoA1 variants were estimated by measuring background-subtracted fluorescence around the *C. elegans* nerve ring. Dorsal nerve cords were imaged to determine synaptic and axonal distribution of rEndoA1 variants. Fluorescence images were analyzed using custom software in IGOR Pro (WaveMetrics, Lake Oswego, OR) (Dittman and Kaplan, 2006, Burbea et al., 2002). Images of fluorescent slides (Chroma Technology Group, VT) were collected daily to monitor the laser stability, and the dorsal cord fluorescence was normalized to the slide fluorescence value. Statistical significance was determined using one-way ANOVA or Student's t-test and all values reported are means ± SEM.

VGLUT-pHluorin Imaging and Analysis

Worms carrying the *kyIs673* [*sra-6p::eat-4::pHluorin*] transgene were used for imaging VGLUT-pHluorin fluorescence as previously described (Ventimiglia and Bargmann, 2017). Animals were loaded into custom-built PDMS microfluidic chambers designed to deliver stimuli under a fluorescent microscope (Chronis et al., 2007). To prevent movement, animals were paralyzed with 1mM tetramisole hydrochloride. NaCl stimulus (500mM) was prepared fresh daily in S. Basal Buffer. The ASH axons were imaged on an inverted Leica DMi8 microscope through a Leica PL APO 63x 1.40 NA oil immersion objective, onto an Andor iXon Life 888 EMCCD camera, using Leica LAS-X software. Animals were allowed to acclimate for 5 minutes in microfluidic chambers before imaging, and were adapted to blue light for 90 seconds. No more than 3 trials were performed per animal. The time duration for all recording trials was 100 seconds, and the stimulus was presented for 10 seconds, starting at 30 seconds after imaging began. Images were captured at 5 frames per second.

Imaging analysis was performed as previously described (Ventimiglia and Bargmann, 2017). Briefly, images were corrected for x-y drift, and images with substantial z-drift were discarded. The axon was divided into 3x3 pixel ROIs by hand, and background ROIs to the left and right of each axon ROI were selected. Intensity and pixel measurements of the axon and background were extracted from those ROIs. Background and bleaching artifacts were corrected. VGLUT-pHluorin has slow bleaching kinetics,

whereas the background exhibits significant bleaching. To correct for this, background bleaching was linearly modeled through a 'polyfit' function in MATLAB and the linear fit was subtracted from the background signal. After bleaching correction, background correction was performed by subtracting fluctuations in the background signal from the fluorescence traces. Basal fluorescence of VGLUT-pHluorin was obtained by averaging the first 10 seconds of each ROI for each trial after background correction. Decay curves were fitted and $\Delta F/F$ was determined as previously described. All imaging experiments for a given condition or observation were repeated on at least two separate days using independently prepared buffers and stimuli. The number of trials per animal and the total number of animals are reported along with the total trial number in the figure legends.

Bafilomycin Treatment

Bafilomycin A1 (BafA) was dissolved in DMSO to a stock concentration of 25 mM. A 5 µM BafA working solution was prepared using M9 buffer. Day-1 adult worms carrying VGLUT-pHluorin were added to 50 µl of BafA working solution. After 1 hour of BafA treatment, the ASH axons were imaged on an inverted Leica DMi8 microscope through a Leica PL APO 40x 1.10 NA water immersion objective, onto an Andor iXon Life 888 EMCCD camera, using Leica LAS-X software.

Liposome Preparation

Lipids were stored at −20°C. POPC (1-palmitoyl-2-oleoyl-sn-glycero-3-phosphocholine, designated as PC) was purchased from Larodan Inc, DOPS (1,2-di-oleoyl-sn-glycero-3-phospho-l-serine, designated as PS) was obtained from NOF America Corporation, and PI(4,5)P2 (brain L-α-phosphatidylinositol-4,5-bisphosphate, designated as PIP2) was purchased from Avanti Polar Lipids. Lipids dissolved in chloroform were mixed in a glass tube. The lipid mixture was dried under a stream of nitrogen gas for 30 min, and residual solvent was removed under vacuum (Labconco Free Zone 2.5 lyophilizer) for 2 hours. The dried lipid film was then rehydrated in the HEPES buffer (50 mM HEPES, 150 mM NaCl, pH 7.4), followed by a brief sonication to homogenize the mixture. The resulting lipid suspension was then extruded 21 times through 200 nm pore-size polycarbonate membranes, using a Mini extruder (Avanti Polar lipids) to form unilamellar vesicles.

Transmission Electron Microscope for Visualizing Synaptic Vesicle

Approximately 10 adult hermaphrodites were quickly loaded into a 100 µm freezing chamber containing space-filling bacteria. These worms were frozen instantaneously at ~ -180 ºC in a Leica EM PACT2 system. The frozen worms were fixed in a Leica EM AFS2 machine using 1% osmium in 0.1% UA in acetone fixative, then embedded in Eponate 12 from Ted Pella, Inc. Serial sections were cut at a thickness of 40 nm using an ultracut E microtome, collected on pioloform-covered slotted grids (notchnum 1x2 mm oval) from Ted Pella, Inc., and counterstained in 6% aqueous uranyl acetate for 1.5 hrs, followed by Reynolds lead citrate for 7 min. Images were obtained on a Talos L120C TEM transmission electron microscope (Thermo Fisher Scientific Inc, USA) operating at 120KV. Micrographs were collected using the Ceta-M 4k x 4k high-resolution camera (Thermo Fisher Scientific Inc, USA). Synapse profiles were used to count the number of SVs. Each profile represents a single section that passes through the dense projection. P values were generated using one-way ANOVA followed by Dunnett's test.

Electrophysiology

Day-1 young adult hermaphrodite *C. elegans* were dissected as previously described (Richmond et al., 1999, Dong et al., 2015). Animals were immobilized on Sylgard-coated coverslips using tissue adhesive glue (Histoacryl Blue, Braun), and were dissected in extracellular solution via a dorsolateral incision using a sharpened tungsten needle. After removing gonad and intestines by suction through a glass pipette, the cuticle flap was turned and gently glued down to expose the underlying ventral nerve cord and body-wall-muscle quadrants. The worm prep was then mounted onto a fixed-stage upright microscope (BX51WI, Olympus) equipped with a 60x water-immersion objective lens. The integrity of the anterior ventral body wall muscle and the ventral nerve cord were visually examined via the DIC microscopy, and ventral muscle cells were patched using fire-polished 2-5 MΩ resistant borosilicate pipettes (World Precision Instruments, USA). Whole-cell patch clamp recordings were carried out at 20°C. Body-wall muscle cells were voltage clamped at -60 mV to record postsynaptic currents. The currents were recorded in the whole-cell configuration from muscle cells using an amplifier (EPC-10; HEKA, Germany). Extracellular solution contained (in mM) 150 NaCl, 5 KCl, 1 CaCl2, 5 MgCl2, 10 glucose and 10 HEPES, titrated to pH

7.3 with NaOH, 330 mOsm with sucrose. Internal solution contained 135 CH3O3SCs, 5 CsCl, 5 MgCl2, 5 EGTA, 0.25 CaCl2, 10 HEPES and 5 Na2ATP, adjusted to pH 7.2 using CsOH. Evoked EPSC responses were induced by applying a 0.4 ms, 30 μA pulse, generated by a stimulus isolator (A365, WPI), through a borosilicate pipette (~2 MΩ) placed in close apposition to the ventral nerve cord. Series resistance was compensated to 70% for the evoked EPSC recording. All chemicals were purchased from Sigma. Data were sampled at 10 kHz using Patchmaster (HEKA), following low-pass filtering at 2 kHz. The number of animals for each experiment was specified in Figure legends.

Alignment of Protein Sequences

For each amphipathic helix-containing protein (EndoA1 – *R. norvegicus*, NP_446387; KES1 – *S. cerevisiae*, NP_015180; Nup133 – *H. sapiens*, NP_060700), the helix sequence, plus 50 amino acids on either end, where possible (some helices were terminal), was used as a BLASTP query to identify orthologs within the NR database. These longer protein sequences were aligned using MAFFT (PMID: 12136088), and the aligned helix sequences were extracted. For each set of helix sequences, sequences annotated as the gene of interest were extracted, and splice isoforms and duplicate sequences were removed to generate an alignment with a single sequence from each sampled species. Logo plots were generated using Geneious Prime 2021.1. Net charge was calculated for each helix using established amino acid properties at physiological pH.

Negative-Stain Electron Microscopy

Sample preparation for negative stain was carried out as previously described with modifications (Farsad et al., 2001, Poudel et al., 2016). Briefly, liposomes (total lipids 2 mM, 0.2 μm in diameter) were incubated with endophilin variants (4 μM) in the HEPES buffer (50mM HEPES, 150 mM NaCl, pH7.4) for 5 min at room temperature. Copper grids were glow-discharged for 40 seconds, after which grids were incubated with samples for 2 minutes. Samples were fixed using 0.5x Karnovsky's fix. Grids were then washed with 1 drop of 0.1 M cacodylate buffer, followed with a 4 drop H_2O wash. A drop of 1% uranyl acetate was touched on the sample. The grids were then carefully dragged through dry filter papers and put in a desiccator overnight to dry. Images were collected using JEOL TEM 1400 and Talos L120C Transmission

Electron Microscopes. All measurements were made using ImageJ. Ten images were selected for analysis by following random number tables generated by Google Sheets.

Quantification and Statistical Analysis

One-way ANOVA followed by Tukey or Dunnett's test was used for multiple comparisons. $p < 0.05$ was considered to be statistically significant (*$p < 0.05$, **$p < 0.01$, ***$p < 0.001$). Statistical analysis and graphing were carried out using Prism8 (GraphPad), Igor Pro (WaveMetrics), Clampfit (Molecular Devices), FluoView (Olympus), and Excel (Microsoft). Data were presented as the mean ± standard error (SEM). The sample size and significance test of statistical analyses were indicated in the figure legends. A *p*-value lower than 0.05 was considered statistically significant.

Table S1. Detailed information on Experimental Models: Organisms/Strains. Related to Figure 1-7.

Table S2. Detailed information on Recombinant DNA. Related to Figure 1-7.

Chapter 3. Research Progress Report

De Novo Engineering of Functional Amphipathic Motifs

3.1 Overview

Amphipathic motifs are key regulators of membrane trafficking, including secretory vesicle exocytosis and endocytosis (Drin and Antonny, 2010; Antonny, 2011; Vanni et al., 2013). We previously showed that the endophilin H0 motif, a 20-residue amphipathic helix at the N-terminus of endophilin (Figure 1), is essential for synaptic vesicle recycling in vivo (Zhang et al., 2022). This motif senses both membrane curvature and electrostatic charge, suggesting that its short amino acid sequence encodes specific biochemical features essential for function in cells. But what are these features, and how are they encoded in sequence? To address this, we took a new approach: rather than identifying necessary elements through loss-of-function analysis, we sought to define the sufficient features by designing de novo amphipathic motifs with functional activity in vivo.

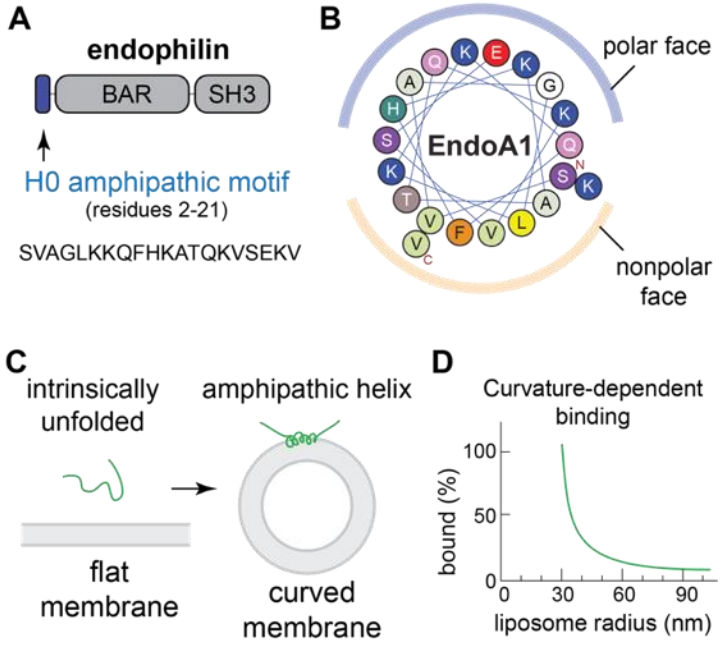

Figure 2. 1. Endophilin features an N-terminal amphipathic helix, H0.
(A) The schematic diagram illustrates the domain structure of endophilin. The amino acid sequence of the H0 motif (residues 2-21) of rat endophilin A1 (rEndoA1) is shown at the bottom. **(B)** A helical wheel presentation of the H0 motif, with amino acid residues color-coded by type. The polar and nonpolar faces of the H0 helix are indicated. **(C)** In solution, H0 is an intrinsically unfolded sequence (*left*). Upon contact with curved membranes, it folds into an amphipathic helix on the surface of highly curved membranes (*right*), with residues on the nonpolar face embedded within the membrane hydrophobic core and residues on the polar face oriented toward the aqueous cytoplasm. **(D)** The interaction of endophilin H0 with membranes depends on the degree of membrane curvature. Panels C and D are modified from Antonny B., 2011.

3.2 Significance and Research Progress

As Richard Feynman famously stated, "What I cannot create, I do not understand." This principle motivates our use of a synthetic biology approach to investigate curvature-sensing amphipathic motifs. Rather than relying solely on naturally evolved proteins, which often contain complex, overlapping regulatory features, we construct simplified, rationally designed synthetic motifs to isolate the essential characteristics sufficient for their function.

Our study revealed that amphipathic helices with similar curvature-sensing behavior in vitro can differ in their biochemical requirements for function. These observations highlight the need for approaches that can dissect specific sequence and structural features independently. Synthetic biology provides such a framework by enabling systematic, reductionist analysis of motif architecture through rational design and controlled testing. Engineered amphipathic helices can be tailored with defined electrostatic and hydrophobic profiles and introduced into minimal sequence backgrounds, allowing us to determine which properties govern membrane curvature-sensing and function. These designed motifs reduce the ambiguity caused by confounding sequence and structural dependencies in natural proteins, allowing clearer attribution of observed phenotypes to specific motif features.

Moreover, synthetic biology facilitates the exploration of curvature-sensing motifs not as isolated elements but as modular components within broader protein architectures. This modularity opens the door for fine-tuned regulation of membrane remodeling events, such as vesicle endocytosis and exocytosis, by enabling precise experimental control over motif behavior, localization, and interaction profiles. Through this lens, amphipathic helices can be optimized to function under specific physiological conditions, and novel motifs can be tailored for distinct trafficking roles.

Through our work in progress, we successfully identified engineered synthetic amphipathic helices that can support endophilin in vivo. Our study has showed that deletion of the H0 motif from endophilin (ΔH0) resembled locomotion defects in endophilin null mutant C. elegans (Figure 2C). Building on this result, we engineered a functional endophilin chimera by replacing the native H0 motif with a designed 8-residue amphipathic sequence (syn 8aa, Fig 2A-B), which composed with only three types of amino acid: isoleucine (I), lysine (K), and tryptophan (W). Neuronal expression of this endophilin chimera (snb-1p::KIWKKIIK_rEndoA1::gfp) via a single-copy transgene significantly rescued locomotion defects in

endophilin-null worms (Figure 2C). These results demonstrate the first designed amphipathic helix with simple amino acid sequence that can support endophilin function in vivo.

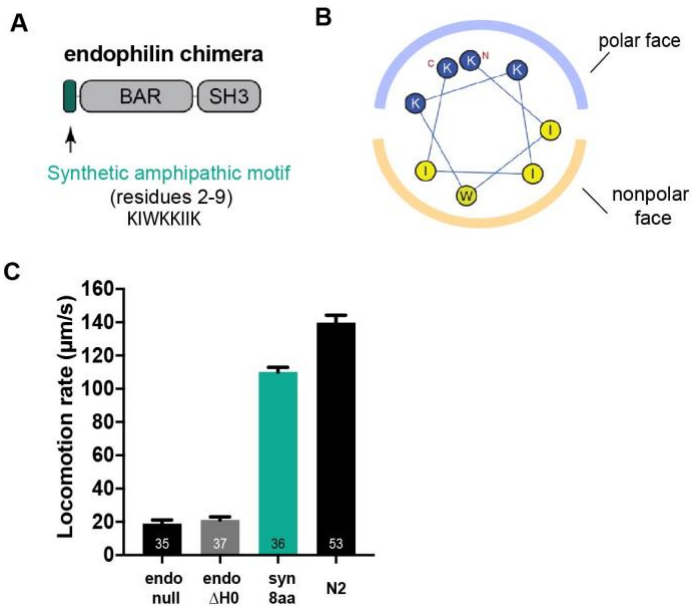

Figure 2. 2. Endophilin features a synthetic amphipathic helix.
(A) The schematic diagram illustrates the domain structure of endophilin chimera. The amino acid sequence of the synthetic amphipathic motif (residues 2-9) of engineered rat endophilin A1 chimera (rEndoA1) is shown at the bottom. **(B)** A helical wheel presentation of the synthetic amphipathic motif, with amino acid residues color-coded by type. The polar and nonpolar faces of the helix are indicated. **(C)** Summary data for locomotion rates. The number of worms analyzed for each genotype was indicated in the bar graphs, and error bars represent standard error of the mean (SEM).

In summary, synthetic biology offers an experimentally tractable strategy to uncover the design logic behind amphipathic motif specificity. By combining rational design with in vivo validation, we are well positioned to advance our understanding of curvature-sensing mechanisms and translate these insights into novel tools for cellular engineering and neurobiology.

3.3 Future Directions

3.3.1 Systematic Mutational Scanning to Define Design Principles

To identify the minimal biochemical determinants required for functional motif design, we have initiated a comprehensive mutational scan across synthetic amphipathic helices. Each residue is systematically mutated to assess its contribution to membrane interaction and endocytic activity. This approach will allow us to generate a high-resolution map correlating specific residues with functional phenotypes, and will help resolve which features (e.g., side-chain size, charge, polarity) drive membrane targeting versus activity.

The resulting dataset will serve as a blueprint for generating a predictive framework for amphipathic motif function. Such a framework can guide the design of tailored motifs with predictable behaviors across membrane compartments.

3.3.2 Functional Tuning of Vesicle Dynamics through Engineered Motifs

Engineered motifs with various curvature-sensitive levels will be expressed in neuronal systems to modulate the balance between exocytosis and endocytosis. This approach will help us assess whether amphipathic helices can serve as tools to fine-tune vesicle cycle kinetics, a potential avenue for correcting the disruptions in the coupling between exocytosis and endocytosis. This disruption is often seen in neurological disorders, where vesicle turnover is dysregulated.

Our study laid the groundwork for understanding motif-specific contributions to membrane curvature sensing in vivo. Our work has revealed that functional specificity can be engineered into amphipathic motifs through targeted modifications of biochemical properties, rather than by mimicking natural sequences. This insight unlocks new possibilities in synthetic biology, allowing the design of customizable curvature-sensing elements that can regulate distinct membrane remodeling pathways.

Our current and future research will expand on this foundation to construct predictive models of motif function, identify transferable design principles, and deploy synthetic motifs to interrogate and modulate membrane trafficking in diverse biological systems. These advances not only enhance our

understanding of membrane biophysics but also offer translational potential for diseases associated with dysfunctional vesicle dynamics.

Bibliography

ALECU, I. & BENNETT, S.A.L. 2019. Dysregulated lipid metabolism and its role in α-synucleinopathy in Parkinson's disease, *Frontiers in Neuroscience*, 13, p. 328. doi:10.3389/fnins.2019.00328.

AMBROSO, M. R., HEGDE, B. G. & LANGEN, R. 2014. Endophilin A1 induces different membrane shapes using a conformational switch that is regulated by phosphorylation. *Proc Natl Acad Sci U S A,* 111**,** 6982-7.

ANTONNY, B. 2011. Mechanisms of membrane curvature sensing. *Annu Rev Biochem,* 80**,** 101-23.

BAI, J. H., HU, Z. T., DITTMAN, J. S., PYM, E. C. G. & KAPLAN, J. M. 2010. Endophilin Functions as a Membrane-Bending Molecule and Is Delivered to Endocytic Zones by Exocytosis. *Cell,* 143**,** 430-441.

BALLA, T. 2013. Phosphoinositides: tiny lipids with giant impact on cell regulation. *Physiol Rev,* 93**,** 1019-137.

BARTELS, T., AHLSTROM, L. S., LEFTIN, A., KAMP, F., HAASS, C., BROWN, M. F. & BEYER, K. 2010. The N-terminus of the intrinsically disordered protein alpha-synuclein triggers membrane binding and helix folding. *Biophys J,* 99**,** 2116-24.

BHATIA, V. K., MADSEN, K. L., BOLINGER, P. Y., KUNDING, A., HEDEGARD, P., GETHER, U. & STAMOU, D. 2009. Amphipathic motifs in BAR domains are essential for membrane curvature sensing. *EMBO J,* 28**,** 3303-14.

BIGAY, J. & ANTONNY, B. 2012. Curvature, lipid packing, and electrostatics of membrane organelles: defining cellular territories in determining specificity. *Dev Cell,* 23**,** 886-95.

BIGAY, J., CASELLA, J. F., DRIN, G., MESMIN, B. & ANTONNY, B. 2005. ArfGAP1 responds to membrane curvature through the folding of a lipid packing sensor motif. *Embo Journal,* 24**,** 2244-2253.

BLOOD, P. D., SWENSON, R. D. & VOTH, G. A. 2008. Factors influencing local membrane curvature induction by N-BAR domains as revealed by molecular dynamics simulations. *Biophysical Journal,* 95**,** 1866-1876.

BOUCROT, E., FERREIRA, A. P. A., ALMEIDA-SOUZA, L., DEBARD, S., VALLIS, Y., HOWARD, G., BERTOT, L., SAUVONNET, N. & MCMAHON, H. T. 2015. Endophilin marks and controls a clathrin-independent endocytic pathway. *Nature,* 517**,** 460-+.

BOUCROT, E., PICK, A., CAMDERE, G., LISKA, N., EVERGREN, E., MCMAHON, H. T. & KOZLOV, M. M. 2012. Membrane fission is promoted by insertion of amphipathic helices and is restricted by crescent BAR domains. *Cell,* 149**,** 124-36.

BRAUN, A. R., LACY, M. M., DUCAS, V. C., RHOADES, E. & SACHS, J. N. 2017. alpha-Synuclein's Uniquely Long Amphipathic Helix Enhances its Membrane Binding and Remodeling Capacity. *J Membr Biol,* 250**,** 183-193.

BURBEA, M., DREIER, L., DITTMAN, J. S., GRUNWALD, M. E. & KAPLAN, J. M. 2002. Ubiquitin and AP180 regulate the abundance of GLR-1 glutamate receptors at postsynaptic elements in C. elegans. *Neuron,* 35**,** 107-20.

CAMPELO, F., MCMAHON, H. T. & KOZLOV, M. M. 2008. The hydrophobic insertion mechanism of membrane curvature generation by proteins. *Biophys J,* 95**,** 2325-39.

CAPRARO, B. R., SHI, Z., WU, T. T., CHEN, Z. M., DUNN, J. M., RHOADES, E. & BAUMGART, T. 2013. Kinetics of Endophilin N-BAR Domain Dimerization and Membrane Interactions. *Journal of Biological Chemistry,* 288**,** 12533-12543.

CESTRA G., CASTAGNOLI, L., DENTE, L., MINENKOVA, O., PETRELLI, A., MIGONE, N., HOFFMULLER, U., SCHNEIDER-MERGENER, J. & CESARENI, G. 1999. The SH3 domains of endophilin and amphiphysin bind to the proline-rich region of synaptojanin 1 at distinct sites that display an unconventional binding specificity. *J. Biol. Chem.*, 274, 32001–32007.

CHEN, Z., ATEFI, E. & BAUMGART, T. 2016a. Membrane Shape Instability Induced by Protein Crowding. *Biophys J,* 111**,** 1823-1826.

CHEN, Z., CHANG, K., CAPRARO, B. R., ZHU, C., HSU, C. J. & BAUMGART, T. 2014. Intradimer/Intermolecular interactions suggest autoinhibition mechanism in endophilin A1. *J Am Chem Soc,* 136**,** 4557-64.

CHEN, Z., ZHU, C., KUO, C. J., ROBUSTELLI, J. & BAUMGART, T. 2016b. The N-Terminal Amphipathic Helix of Endophilin Does Not Contribute to Its Molecular Curvature Generation Capacity. *Journal of the American Chemical Society,* 138**,** 14616-14622.

CHRONIS, N., ZIMMER, M. & BARGMANN, C. I. 2007. Microfluidics for in vivo imaging of neuronal and behavioral activity in Caenorhabditis elegans. *Nat Methods,* 4**,** 727-31.

CLAYTON, E. L. & COUSIN, M. A. 2009. The molecular physiology of activity-dependent bulk endocytosis of synaptic vesicles. *J Neurochem,* 111**,** 901-14.

COPIC, A., ANTOINE-BALLY, S., GIMENEZ-ANDRES, M., LA TORRE GARAY, C., ANTONNY, B., MANNI, M. M., PAGNOTTA, S., GUIHOT, J. & JACKSON, C. L. 2018. A giant amphipathic helix from a perilipin that is adapted for coating lipid droplets. *Nat Commun,* 9**,** 1332.

CORNELL, R. B. & TANEVA, S. G. 2006. Amphipathic helices as mediators of the membrane interaction of amphitropic proteins, and as modulators of bilayer physical properties. *Curr Protein Pept Sci,* 7**,** 539-52.

CUI, H., LYMAN, E. & VOTH, G. A. 2011. Mechanism of membrane curvature sensing by amphipathic helix containing proteins. *Biophys J,* 100**,** 1271-9.

CUI, H., MIM, C., VAZQUEZ, F. X., LYMAN, E., UNGER, V. M. & VOTH, G. A. 2013. Understanding the role of amphipathic helices in N-BAR domain driven membrane remodeling. *Biophys J,* 104**,** 404-11.

DAVIDSON, W. S., JONAS, A., CLAYTON, D. F. & GEORGE, J. M. 1998. Stabilization of alpha-synuclein secondary structure upon binding to synthetic membranes. *Journal of Biological Chemistry,* 273**,** 9443-9449.

DI PAOLO, G. & DE CAMILLI, P. 2006. Phosphoinositides in cell regulation and membrane dynamics. *Nature,* 443**,** 651-7.

DICKMAN, D. K., HORNE, J. A., MEINERTZHAGEN, I. A. & SCHWARZ, T. L. 2005. A slowed classical pathway rather than kiss-and-run mediates endocytosis at synapses lacking synaptojanin and endophilin. *Cell,* 123**,** 521-533.

DITTMAN, J. S. & KAPLAN, J. M. 2006. Factors regulating the abundance and localization of synaptobrevin in the plasma membrane. *Proc Natl Acad Sci U S A,* 103**,** 11399-404.

DONG, Y. M., GOU, Y. Y., LI, Y., LIU, Y. & BAI, J. H. 2015. Synaptojanin cooperates in vivo with endophilin through an unexpected mechanism. *Elife,* 4.

DOUCET, C. M., ESMERY, N., DE SAINT-JEAN, M. & ANTONNY, B. 2015. Membrane Curvature Sensing by Amphipathic Helices Is Modulated by the Surrounding Protein Backbone. *PLoS One,* 10**,** e0137965.

DOUCET, C. M., TALAMAS, J. A. & HETZER, M. W. 2010. Cell cycle-dependent differences in nuclear pore complex assembly in metazoa. *Cell,* 141**,** 1030-41.

DRIN, G. & ANTONNY, B. 2010. Amphipathic helices and membrane curvature. *FEBS Lett,* 584**,** 1840-7.

DRIN, G., CASELLA, J. F., GAUTIER, R., BOEHMER, T., SCHWARTZ, T. U. & ANTONNY, B. 2007. A general amphipathic alpha-helical motif for sensing membrane curvature. *Nature Structural & Molecular Biology,* 14**,** 138-146.

FARSAD, K., RINGSTAD, N., TAKEI, K., FLOYD, S. R., ROSE, K. & DE CAMILLI, P. 2001. Generation of high curvature membranes mediated by direct endophilin bilayer interactions. *Journal of Cell Biology,* 155**,** 193-200.

FERREIRA, A. P. A. & BOUCROT, E. 2018. Mechanisms of Carrier Formation during Clathrin-Independent Endocytosis. *Trends Cell Biol,* 28**,** 188-200.

FLETCHER, D.A. AND MULLINS, R.D., 2010. Cell mechanics and the cytoskeleton. *Nature*, 463(7280), pp.485–492. doi:10.1038/nature08908.

FORD, M. G. J., MILLS, I. G., PETER, B. J., VALLIS, Y., PRAEFCKE, G. J. K., EVANS, P. R. & MCMAHON, H. T. 2002. Curvature of clathrin-coated pits driven by epsin. *Nature,* 419**,** 361-366.

FROKJAER-JENSEN, C., DAVIS, M. W., AILION, M. & JORGENSEN, E. M. 2012. Improved Mos1-mediated transgenesis in C. elegans. *Nat Methods,* 9**,** 117-8.

FROKJAER-JENSEN, C., DAVIS, M. W., HOPKINS, C. E., NEWMAN, B. J., THUMMEL, J. M., OLESEN, S. P., GRUNNET, M. & JORGENSEN, E. M. 2008. Single-copy insertion of transgenes in Caenorhabditis elegans. *Nat Genet,* 40**,** 1375-83.

GALIC, M., JEONG, S., TSAI, F. C., JOUBERT, L. M., WU, Y. I., HAHN, K. M., CUI, Y. & MEYER, T. 2012. External push and internal pull forces recruit curvature-sensing N-BAR domain proteins to the plasma membrane. *Nat Cell Biol,* 14**,** 874-81.

GALLOP, J. L., JAO, C. C., KENT, H. M., BUTLER, P. J. G., EVANS, P. R., LANGEN, R. & T MCMAHON, H. 2006. Mechanism of endophilin N-BAR domain-mediated membrane curvature. *Embo Journal,* 25**,** 2898-2910.

GEORGIEVA, E. R., RAMLALL, T. F., BORBAT, P. P., FREED, J. H. & ELIEZER, D. 2008. Membrane-bound alpha-synuclein forms an extended helix: long-distance pulsed ESR measurements using vesicles, bicelles, and rodlike micelles. *J Am Chem Soc,* 130**,** 12856-7.

GIBSON, D. G., YOUNG, L., CHUANG, R. Y., VENTER, J. C., HUTCHISON, C. A., 3RD & SMITH, H. O. 2009. Enzymatic assembly of DNA molecules up to several hundred kilobases. *Nat Methods,* 6**,** 343-5.

GIMENEZ-ANDRES, M., COPIC, A. & ANTONNY, B. 2018. The Many Faces of Amphipathic Helices. *Biomolecules,* 8.

GOLDBERG, J. 1998. Structural basis for activation of ARF GTPase: mechanisms of guanine nucleotide exchange and GTP-myristoyl switching. *Cell,* 95**,** 237-48.

GONZALEZ-RUBIO, P., GAUTIER, R., ETCHEBEST, C. & FUCHS, P. F. 2011. Amphipathic-Lipid-Packing-Sensor interactions with lipids assessed by atomistic molecular dynamics. *Biochim Biophys Acta,* 1808**,** 2119-27.

GUDHETI, M.V., MLODZIANOSKI, M. AND HESS, S.T. 2007. Imaging and shape analysis of GUVs as model plasma membranes: effect of trans DOPC on membrane properties, *Biophysical Journal*, 93(6), pp. 2011–2023. doi:10.1529/biophysj.106.103374.

HATZAKIS, N. S., BHATIA, V. K., LARSEN, J., MADSEN, K. L., BOLINGER, P. Y., KUNDING, A. H., CASTILLO, J., GETHER, U., HEDEGARD, P. & STAMOU, D. 2009. How curved membranes recruit amphipathic helices and protein anchoring motifs. *Nat Chem Biol,* 5**,** 835-41.

HEMPEL, A. M., WANG, S. B., LETEK, M., GIL, J. A. & FLARDH, K. 2008. Assemblies of DivIVA mark sites for hyphal branching and can establish new zones of cell wall growth in Streptomyces coelicolor. *J Bacteriol,* 190**,** 7579-83.

HIGUCHI, R., KRUMMEL, B. & SAIKI, R. K. 1988. A general method of in vitro preparation and specific mutagenesis of DNA fragments: study of protein and DNA interactions. *Nucleic Acids Res,* 16**,** 7351-67.

HILL, S. E. & COLON-RAMOS, D. A. 2020. The Journey of the Synaptic Autophagosome: A Cell Biological Perspective. *Neuron,* 105**,** 961-973.

HOOPMANN, P., PUNGE, A., BARYSCH, S. V., WESTPHAL, V., BUCKERS, J., OPAZO, F., BETHANI, I., LAUTERBACH, M. A., HELL, S. W. & RIZZOLI, S. O. 2010. Endosomal sorting of readily releasable synaptic vesicles. *Proc Natl Acad Sci U S A,* 107**,** 19055-60.

HRISTOVA, K., WIMLEY, W. C., MISHRA, V. K., ANANTHARAMIAH, G. M., SEGREST, J. P. & WHITE, S. H. 1999. An amphipathic alpha-helix at a membrane interface: A structural study using a novel X-ray diffraction method. *Journal of Molecular Biology,* 290**,** 99-117.

IM, Y. J., RAYCHAUDHURI, S., PRINZ, W. A. & HURLEY, J. H. 2005. Structural mechanism for sterol sensing and transport by OSBP-related proteins. *Nature,* 437**,** 154-158.

JAO, C. C., DER-SARKISSIAN, A., CHEN, J. & LANGEN, R. 2004. Structure of membrane-bound α-synuclein studied by site-directed spin labeling. *Proceedings of the National Academy of Sciences of the United States of America,* 101**,** 8331.

JAO, C. C., HEGDE, B. G., CHEN, J., HAWORTH, I. S. & LANGEN, R. 2008. Structure of membrane-bound alpha-synuclein from site-directed spin labeling and computational refinement. *Proc Natl Acad Sci U S A,* 105**,** 19666-71.

JAO, C. C., HEGDE, B. G., GALLOP, J. L., HEGDE, P. B., MCMAHON, H. T., HAWORTH, I. S. & LANGEN, R. 2010. Roles of amphipathic helices and the bin/amphiphysin/rvs (BAR) domain of endophilin in membrane curvature generation. *J Biol Chem,* 285**,** 20164-70.

JARSCH, I. K., DASTE, F. & GALLOP, J. L. 2016. Membrane curvature in cell biology: An integration of molecular mechanisms. *J Cell Biol,* 214**,** 375-87.

JENSEN, M.B., BHATIA, V.K., JAO, C.C., RASMUSSEN, J.E., PEDERSEN, S.L., JENSEN, K.J., LANGEN, R. AND STAMOU, D. 2011. Membrane curvature sensing by amphipathic helices: a single liposome study using α-synuclein and annexin B12, *Journal of Biological Chemistry*, 286(49), pp. 42603–42614. doi:10.1074/jbc.M111.271130.

KAISER, E. T. & KEZDY, F. J. 1983. Secondary structures of proteins and peptides in amphiphilic environments. (A review). *Proc Natl Acad Sci U S A,* 80**,** 1137-43.

KAISER, E. T. & KEZDY, F. J. 1984. Amphiphilic secondary structure: design of peptide hormones. *Science,* 223**,** 249-55.

KANEKO, T., MAEDA, A., TAKEFUJI, M., AOYAMA, H., NAKAYAMA, M., KAWABATA, S., KAWANO, Y., IWAMATSU, A., AMANO, M. & KAIBUCHI, K. 2005. Rho mediates endocytosis of epidermal growth factor receptor through phosphorylation of endophilin A1 by Rho-kinase. *Genes Cells,* 10**,** 973-87.

KARANASIOS, E., HAN, G. S., XU, Z., CARMAN, G. M. & SINIOSSOGLOU, S. 2010. A phosphorylation-regulated amphipathic helix controls the membrane translocation and function of the yeast phosphatidate phosphatase. *Proc Natl Acad Sci U S A,* 107**,** 17539-44.

KITTELMANN, M., LIEWALD, J. F., HEGERMANN, J., SCHULTHEIS, C., BRAUNER, M., STEUER COSTA, W., WABNIG, S., EIMER, S. & GOTTSCHALK, A. 2013. In vivo synaptic recovery following optogenetic hyperstimulation. *Proc Natl Acad Sci U S A,* 110**,** E3007-16.

KONONENKO, N. L. & HAUCKE, V. 2015. Molecular mechanisms of presynaptic membrane retrieval and synaptic vesicle reformation. *Neuron,* 85**,** 484-96.

KONONENKO, NATALIA L., PUCHKOV, D., CLASSEN, GALA A., WALTER, ALEXANDER M., PECHSTEIN, A., SAWADE, L., KAEMPF, N., TRIMBUCH, T., LORENZ, D., ROSENMUND, C., MARITZEN, T. & HAUCKE, V. 2014. Clathrin/AP-2 Mediate Synaptic Vesicle Reformation from Endosome-like Vacuoles but Are Not Essential for Membrane Retrieval at Central Synapses. *Neuron,* 82**,** 981-988.

KOZLOV, M.M., MCMAHON, H.T. AND CHERNOMORDIK, L.V. 2014. Protein-driven membrane stresses in fusion and fission, *Trends in Biochemical Sciences*, 39(9), pp. 541–552.

KRAUSS, M., JIA, J. Y., ROUX, A., BECK, R., WIELAND, F. T., DE CAMILLI, P. & HAUCKE, V. 2008. Arf1-GTP-induced tubule formation suggests a function of Arf family proteins in curvature acquisition at sites of vesicle budding. *Journal of Biological Chemistry,* 283**,** 27717-27723.

KROLL, J., TOBON, L. M. J., VOGL, C., NEEF, J., KONDRATIUK, I., KONIG, M., STRENZKE, N., WICHMANN, C., MILOSEVIC, I. & MOSER, T. 2019. Endophilin-A regulates presynaptic Ca2+ influx and synaptic vesicle recycling in auditory hair cells. *Embo Journal,* 38.

LEE, M. C., ORCI, L., HAMAMOTO, S., FUTAI, E., RAVAZZOLA, M. & SCHEKMAN, R. 2005. Sar1p N-terminal helix initiates membrane curvature and completes the fission of a COPII vesicle. *Cell,* 122**,** 605-17.

LENARCIC, R., HALBEDEL, S., VISSER, L., SHAW, M., WU, L. J., ERRINGTON, J., MARENDUZZO, D. & HAMOEN, L. W. 2009. Localisation of DivIVA by targeting to negatively curved membranes. *Embo Journal,* 28**,** 2272-2282.

LOW, C., WEININGER, U., LEE, H., SCHWEIMER, K., NEUNDORF, I., BECK-SICKINGER, A. G., PASTOR, R. W. & BALBACH, J. 2008. Structure and dynamics of helix-0 of the N-BAR domain in lipid micelles and bilayers. *Biophys J,* 95**,** 4315-23.

LUTZMANN, M., KUNZE, R., BUERER, A., AEBI, U. & HURT, E. 2002. Modular self-assembly of a Y-shaped multiprotein complex from seven nucleoporins. *EMBO J,* 21**,** 387-97.

MASUDA, M., TAKEDA, S., SONE, M., OHKI, T., MORI, H., KAMIOKA, Y. & MOCHIZUKI, N. 2006. Endophilin BAR domain drives membrane curvature by two newly identified structure-based mechanisms. *Embo Journal,* 25**,** 2889-2897.

MATTA, S., VAN KOLEN, K., DA CUNHA, R., VAN DEN BOGAART, G., MANDEMAKERS, W., MISKIEWICZ, K., DE BOCK, P. J., MORAIS, V. A., VILAIN, S., HADDAD, D., DELBROEK, L., SWERTS, J., CHAVEZ-GUTIERREZ, L., ESPOSITO, G., DANEELS, G., KARRAN, E., HOLT, M., GEVAERT, K., MOECHARS, D. W., DE STROOPER, B. & VERSTREKEN, P. 2012. LRRK2 controls an EndoA phosphorylation cycle in synaptic endocytosis. *Neuron,* 75**,** 1008-21.

MCLEAN, L. R., HAGAMAN, K. A., OWEN, T. J. & KRSTENANSKY, J. L. 1991. Minimal peptide length for interaction of amphipathic alpha-helical peptides with phosphatidylcholine liposomes. *Biochemistry,* 30**,** 31-7.

MCMAHON, H.T. & BOUCROT, E. 2015. Membrane curvature at a glance, *Journal of Cell Science*, 128(6), pp. 1065–1070. doi:10.1242/jcs.114454.

MCMAHON, H. T. & GALLOP, J. L. 2005. Membrane curvature and mechanisms of dynamic cell membrane remodelling. *Nature,* 438**,** 590-6.

MERCER, J., SCHELHAAS, M. AND HELENIUS, A. 2010, Virus entry by endocytosis*, Annual Review of Biochemistry*, 79, pp. 803–833. doi: 10.1146/annurev-biochem-060208-104626.

MILOSEVIC, I., GIOVEDI, S., LOU, X. L., RAIMONDI, A., COLLESI, C., SHEN, H. Y., PARADISE, S., O'TOOLE, E., FERGUSON, S., CREMONA, O. & DE CAMILLI, P. 2011. Recruitment of Endophilin to Clathrin-Coated Pit Necks Is Required for Efficient Vesicle Uncoating after Fission. *Neuron,* 72**,** 587-601.

MONTENEGRO, G., REBELO, A.P., CONNELL, J., ALLISON, R., BABALINI, C., D'ALOIA, M., MONTIERI, P., SCHÜLE, R., ISHIURA, H., PRICE, J., STRICKLAND, A., GONZALEZ, M.A., BAUMBACH-REARDON, L., DECONINCK, T., HUANG, J., BERNARDI, G., VANCE, J.M., ROGERS, M.T., TSUJI, S., DE JONGHE, P., PERICAK-VANCE, M.A., SCHÖLS, L., ORLACCHIO, A., REID, E. & AND ZÜCHNER, S. 2012. Mutations in the ER-shaping protein reticulon 2 cause the axon-degenerative disorder hereditary spastic paraplegia type 12, *Journal of Clinical Investigation*, 122(2), pp. 538–544. doi:10.1172/JCI60560.

MOSER VON FILSECK, J., VANNI, S., MESMIN, B., ANTONNY, B. & DRIN, G. 2015. A phosphatidylinositol-4-phosphate powered exchange mechanism to create a lipid gradient between membranes. *Nat Commun,* 6**,** 6671.

MURDOCH, J. D., ROSTOSKY, C. M., GOWRISANKARAN, S., ARORA, A. S., SOUKUP, S. F., VIDAL, R., CAPECE, V., FREYTAG, S., FISCHER, A., VERSTREKEN, P., BONN, S., RAIMUNDO, N. & MILOSEVIC, I. 2016. Endophilin-A Deficiency Induces the Foxo3a-Fbxo32 Network in the Brain and Causes Dysregulation of Autophagy and the Ubiquitin-Proteasome System. *Cell Rep,* 17**,** 1071-1086.

NORDEEN, S. A., TURMAN, D. L. & SCHWARTZ, T. U. 2020. Yeast Nup84-Nup133 complex structure details flexibility and reveals conservation of the membrane anchoring ALPS motif. *Nat Commun,* 11**,** 6060.

PETER, B. J., KENT, H. M., MILLS, I. G., VALLIS, Y., BUTLER, P. J., EVANS, P. R. & MCMAHON, H. T. 2004. BAR domains as sensors of membrane curvature: the amphiphysin BAR structure. *Science,* 303**,** 495-9.

POUDEL, K. R., DONG, Y. M., YU, H., SU, A., HO, T., LIU, Y., SCHULTEN, K. & BAI, J. H. 2016. A time course of orchestrated endophilin action in sensing, bending, and stabilizing curved membranes. *Molecular Biology of the Cell,* 27**,** 2119-2132.

POUDEL, K. R., ROH-JOHNSON, M., SU, A., HO, T., MATHSYARAJA, H., ANDERSON, S., GRADY, W. M., MOENS, C. B., CONACCI-SORRELL, M., EISENMAN, R. N. & BAI, J. 2018. Competition between TIAM1 and Membranes Balances Endophilin A3 Activity in Cancer Metastasis. *Dev Cell,* 45**,** 738-752 e6.

PRINZ, W. A. & HINSHAW, J. E. 2009. Membrane-bending proteins. *Crit Rev Biochem Mol Biol,* 44**,** 278-91.

RENARD, H. F., SIMUNOVIC, M., LEMIERE, J., BOUCROT, E., GARCIA-CASTILLO, M. D., ARUMUGAM, S., CHAMBON, V., LAMAZE, C., WUNDER, C., KENWORTHY, A. K., SCHMIDT, A. A., MCMAHON, H. T., SYKES, C., BASSEREAU, P. & JOHANNES, L. 2015. Endophilin-A2 functions in membrane scission in clathrin-independent endocytosis. *Nature,* 517**,** 493-+.

RENARD, H. F., TYCKAERT, F., LO GIUDICE, C., HIRSCH, T., VALADES-CRUZ, C. A., LEMAIGRE, C., SHAFAQ-ZADAH, M., WUNDER, C., WATTIEZ, R., JOHANNES, L., VAN DER BRUGGEN, P., ALSTEENS, D. & MORSOMME, P. 2020. Endophilin-A3 and Galectin-8 control the clathrin-independent endocytosis of CD166. *Nat Commun,* 11**,** 1457.

RICHMOND, J. E., DAVIS, W. S. & JORGENSEN, E. M. 1999. UNC-13 is required for synaptic vesicle fusion in C. elegans. *Nat Neurosci,* 2**,** 959-64.

RINGSTAD, N., NEMOTO, Y. & DECAMILLI, P. 1997. The SH3p4/Sh3p8/SH3p13 protein family: Binding partners for synaptojanin and dynamin via a Grb2-like Src homology 3 domain. *Proceedings of the National Academy of Sciences of the United States of America,* 94**,** 8569-8574.

SARGENT, D. F., BEAN, J. W. & SCHWYZER, R. 1988. Conformation and orientation of regulatory peptides on lipid membranes. Key to the molecular mechanism of receptor selection. *Biophys Chem,* 31**,** 183-93.

SCHUSKE, K. R., RICHMOND, J. E., MATTHIES, D. S., DAVIS, W. S., RUNZ, S., RUBE, D. A., VAN DER BLIEK, A. M. & JORGENSEN, E. M. 2003. Endophilin is required for synaptic vesicle endocytosis by localizing synaptojanin. *Neuron,* 40**,** 749-762.

SHIBATA, Y., HU, J., KOZLOV, M. M. & RAPOPORT, T. A. 2009. Mechanisms shaping the membranes of cellular organelles. *Annu Rev Cell Dev Biol,* 25**,** 329-54.

SNEAD, D., WRAGG, R. T., DITTMAN, J. S. & ELIEZER, D. 2014. Membrane curvature sensing by the C-terminal domain of complexin. *Nat Commun,* 5**,** 4955.

SODT, A. J. & PASTOR, R. W. 2014. Molecular modeling of lipid membrane curvature induction by a peptide: more than simply shape. *Biophys J,* 106**,** 1958-69.

SOUKUP, S. F., KUENEN, S., VANHAUWAERT, R., MANETSBERGER, J., HERNANDEZ-DIAZ, S., SWERTS, J., SCHOOVAERTS, N., VILAIN, S., GOUNKO, N. V., VINTS, K., GEENS, A., DE STROOPER, B. & VERSTREKEN, P. 2016. A LRRK2-Dependent EndophilinA Phosphoswitch Is Critical for Macroautophagy at Presynaptic Terminals. *Neuron,* 92**,** 829-844.

SOUKUP, S. F., VANHAUWAERT, R. & VERSTREKEN, P. 2018. Parkinson's disease: convergence on synaptic homeostasis. *EMBO J,* 37.

STACHOWIAK, J. C., SCHMID, E. M., RYAN, C. J., ANN, H. S., SASAKI, D. Y., SHERMAN, M. B., GEISSLER, P. L., FLETCHER, D. A. & HAYDEN, C. C. 2012. Membrane bending by protein-protein crowding. *Nat Cell Biol,* 14**,** 944-9.

SURESH, S. & EDWARDSON, J. M. 2010. The endophilin N-BAR domain perturbs the structure of lipid bilayers. *Biochemistry,* 49**,** 5766-71.

VAN MEER, G., VOELKER, D. AND FEIGENSON, G. 2008. Membrane lipids: where they are and how they behave, *Nature Reviews Molecular Cell Biology*, 9, pp. 112–124. doi:10.1038/nrm2330.

VANNI, S., VAMPARYS, L., GAUTIER, R., DRIN, G., ETCHEBEST, C., FUCHS, P. F. & ANTONNY, B. 2013. Amphipathic lipid packing sensor motifs: probing bilayer defects with hydrophobic residues. *Biophys J,* 104**,** 575-84.

VAZQUEZ, F. X., UNGER, V. M. & VOTH, G. A. 2013. Autoinhibition of endophilin in solution via interdomain interactions. *Biophys J,* 104**,** 396-403.

VENTIMIGLIA, D. & BARGMANN, C. I. 2017. Diverse modes of synaptic signaling, regulation, and plasticity distinguish two classes of C. elegans glutamatergic neurons. *Elife,* 6.

VERSTREKEN, P., KJAERULFF, O., LLOYD, T. E., ATKINSON, R., ZHOU, Y., MEINERTZHAGEN, I. A. & BELLEN, H. J. 2002. Endophilin Mutations Block Clathrin-Mediated Endocytosis but Not Neurotransmitter Release. *Cell,* 109**,** 101-112.

WANG, Q., KAAN, H. Y., HOODA, R. N., GOH, S. L. & SONDERMANN, H. 2008. Structure and plasticity of Endophilin and Sorting Nexin 9. *Structure,* 16**,** 1574-87.

WATANABE, S., LIU, Q., DAVIS, M. W., HOLLOPETER, G., THOMAS, N., JORGENSEN, N. B. & JORGENSEN, E. M. 2013a. Ultrafast endocytosis at Caenorhabditis elegans neuromuscular junctions. *Elife,* 2.

WATANABE, S., MAMER, L. E., RAYCHAUDHURI, S., LUVSANJAV, D., EISEN, J., TRIMBUCH, T., SOHL-KIELCZYNSKI, B., FENSKE, P., MILOSEVIC, I., ROSENMUND, C. & JORGENSEN, E. M. 2018. Synaptojanin and Endophilin Mediate Neck Formation during Ultrafast Endocytosis. *Neuron,* 98**,** 1184-+.

WATANABE, S., ROST, B. R., CAMACHO-PEREZ, M., DAVIS, M. W., SOHL-KIELCZYNSKI, B., ROSENMUND, C. & JORGENSEN, E. M. 2013b. Ultrafast endocytosis at mouse hippocampal synapses. *Nature,* 504**,** 242-+.

WATANABE, S., TRIMBUCH, T., CAMACHO-PEREZ, M., ROST, B. R., BROKOWSKI, B., SOHL-KIELCZYNSKI, B., FELIES, A., DAVIS, M. W., ROSENMUND, C. & JORGENSEN, E. M. 2014. Clathrin regenerates synaptic vesicles from endosomes. *Nature,* 515**,** 228-U168.

WEISSENHORN, W. 2005. Crystal structure of the endophilin-A1 BAR domain. *J Mol Biol,* 351**,** 653-61.

WRAGG, R. T., SNEAD, D., DONG, Y., RAMLALL, T. F., MENON, I., BAI, J., ELIEZER, D. & DITTMAN, J. S. 2013. Synaptic vesicles position complexin to block spontaneous fusion. *Neuron,* 77**,** 323-34.

YANG, S., PARK, D., MANNING, L., HILL, S. E., CAO, M., XUAN, Z., GONZALEZ, I., DONG, Y., CLARK, B., SHAO, L., OKEKE, I., ALMORIL-PORRAS, A., BAI, J., DE CAMILLI, P. & COLON-RAMOS, D. A. 2022. Presynaptic autophagy is coupled to the synaptic vesicle cycle via ATG-9. *Neuron*.

ZIMMERBERG, J. AND KOZLOV, M.M. 2006. How proteins produce cellular membrane curvature, *Nature Reviews Molecular Cell Biology*, 7(1), pp. 9–19. doi:10.1038/nrm1784.